Visualisation of Quantum Turbulence in Superfluid ^{3}He-B Using a Novel 2D Quasiparticle Detector

Andrew John Woods, MPhys (Hons.)

September 2015

A thesis submitted in fulfilment

of the requirements of the degree of

Doctor of Philosophy

at Lancaster University

Abstract

Quantum turbulence is a conceptually simple form of turbulence, consisting of a tangle of quantised vortex lines. It provides a model system, through which it may be possible to understand features of the complex and not yet fully understood classical turbulence.

A novel detector made from arrays of custom-designed tuning forks was developed and used to investigate properties of excitation beams and quantum turbulence in superfluid ^{3}He-B at temperatures below 200 μK. The detector was constructed from 5 arrays of 5 tuning forks mounted in a copper block to create a 25 pixel square detector of excitation flux. The detector was situated in a cell such that it could be illuminated with a beam of thermal excitations, and that turbulence could be generated in the path of the beam, which will cast a shadow on the face. Characterisation of the detector response to beams generated by the black-body radiator and source wire were performed. We observe that the beam generated by a black-body radiator appears approximately symmetric, consistent with being emitted from a point-source of excitations. In addition to this we find that the profile of the beam generated by the black-body radiator was independent of the power applied to it, an important assumption of the properties of the black-body radiator that had not been previously observed. The beam emitted from a vibrating wire was found to be much narrower and has a angular profile that changes as the velocity of the wire is increased.

Probing a turbulent tangle generated by a vibrating wire with this beam showed that the turbulence appears to fill all of the volume in between the radiator and detector. The vortex line density of the tangle appeared the be greatest in the vicinity of the wire, consistent with previous measurements of the vortex tangle generated by vibrating wires.

In addition, we find that there are reproducible features in the development of the shadow as a function of the wire velocity, indicating that there is some structure in the development. The shadow is independent of the power of the beam used to probe the tangle.

Measurements of fluctuations in the shadow cast by the vortex tangle show that the turbulence has a spectrum reminiscent of the Kolmogorov spectrum. In addition to this the resolution of the detector is such that it is possible in principle to measure the shadow cast by a single vortex line, and we examine candidate events for such a measurement. This represents the first such measurement of the motion of vortex lines in ^{3}He-B.

Declaration

The research performed is a collaborative effort between members of the Low Temperature group at Lancaster University. Data-taking was a collaborative process, however all analysis performed and presented herein is the author's own work. This thesis contains the author's own work which has not been submitted previously for the award of a higher degree at any institution.

Acknowledgements

First and foremost I would like to thank the late Shaun Fisher, who passed away in January 2015, for his guidance and his lectures on Helium-3. Many of the techniques used herein are of his devising and he will be sorely missed.

I would like to thank my supervisor, Viktor Tsepelin, for all of his guidance throughout my PhD. Thanks to to Richard Haley, for always being available to discuss physics-related issues, to George Pickett for his brilliant diagrams and to the other academics in the ULT group for their support.

Furthermore, I would like to thank the postdocs I have worked with, Malcolm Poole and Marcel Človečko, for teaching me how to run a dilution fridge, and for useful discussion and support during data taking and analysis. Thanks to Ed Guise for building and testing the tuning fork part of this detector and to Sean Ahlstrom for keeping the fridge running for almost 3 years.

Thanks to Alan Stokes and Martin Ward for technical support and keeping the lab running, to Tim Clough for running the helium liquefier and to Stephen Holt for building the tuning fork I-V converters. Also thanks go to Steve Holden for keeping the lab equipped and to John Windsor and Rob Lewsey for IT support.

Thanks to all of my fellow PhD students throughout these 3 years, for interesting discussions and great trips to conferences in Japan and Argentina.

Deepest thanks to Mum, my brother, Michael and my Grandparents, for their love and support during my time at University and throughout my life. Thanks also

to my uncle John, who inspired me to go into physics.

Contents

List of Figures

Chapter 1

Introduction

Classical turbulence is well-known for being simultaneously of universal impact whilst being analytically intractable - often called the most important unsolved problem of classical physics [1]. One way forward is to start with a simpler system. A pure superfluid in the zero temperature limit has no viscosity and thus can be considered an ideal fluid. While the flow of bulk superfluid must be irrotational it can mimic classical turbulence by supporting singly quantised vortices. A quantum vortex, at low temperature, provides a concrete example of the thin core vortex filament of the classical fluids literature.

Quantum turbulence consists of a tangle of such quantised vortex lines that interact via their self induced flow, resulting in complex dynamics which may support structures with a large range of length scales. Conceptually, these are very simple conditions in which to study turbulence: since the flow is entirely determined by

the quantised vortex lines, the problem essentially reduces to a study of vortex line motion. These conditions also greatly simplify computer simulations and massively reduce computation times.

Despite the absence of frictional dissipation, quantum turbulence in the zero temperature limit behaves remarkably similarly to classical turbulence and exhibits a Kolmogorov-like energy spectrum. Studies of turbulence in superfluid ^{3}He-B at microkelvin temperatures reveal several advantages over other systems, the most important being that a vortex tangle in this system can be visualized directly via Andreev reflection of ambient thermal excitations [2]. Turbulence in ^{3}He-B can be produced by vibrating wires [3, 4], vibrating grids [5], tuning forks [6], and by rotation of the cryostat [7]. The tangles produced by vibrating wires and grids were probed by Andreev reflection of thermal quasiparticles and quasiparticle beams produced by so-called black-body radiators (BBRs) [8].

The BBR is a very versatile tool in the study of superfluid ^{3}He as it has been shown to be an excellent, highly-sensitive bolometer and a generator of finely-tunable beams of thermal excitations [2, 9, 10]. However, there are still properties of the BBR that are unclear, such as the spatial profile of the excitation beam, and whether the beam spreads as the power applied to it increases. Furthermore, the degree of homogeneity of the turbulence produced by vibrating wires and grids is unknown. Previous measurements were unable to answer that, as turbulence was detected by a handful of vibrating wires or BBRs. Hence, we have designed a 2D quasiparticle detector capable of measuring the spatial variation of the flux

of thermal excitations across it's face with a much higher resolution than previous experiments.

Here we present measurements of the two-dimensional spatial profiles of the thermal excitation beam emitted by a BBR and use such beams to investigate the spatial distribution, statistical properties and development of quantum turbulence generated by a vibrating wire. Furthermore, we have measured the angular spread of the beam generated by a vibrating wire, with a much higher resolution than previous measurements [9].

Conceptually our measurements are carried out as follows: the BBR produces a beam of quasiparticles that illuminates the turbulence produced by a vibrating wire and the shadow cast by the turbulence is measured by our detector. We measure this shadow as a fraction of quasiparticles reflected by the turbulent tangle. The cell layout is shown in figure 1.1 and is described in detail in chapter 3. Here, the key devices are the BBR, the source wire and the tuning fork detector.

The black-body radiator is an approximately cubic box made of stycast-impregnated paper with an orifice in one wall. There are two vibrating wires inside, one used for generating thermal excitations - the heater wire, and the other used to measure the temperature - the thermometer wire. Excitations generated by the heater wire will thermalise inside the box and be emitted in a beam from the orifice. The thermometer wire allows us to calibrate the temperature of the box against the power applied to the heater wire, allowing the use of the box as a sensitive bolometer [9]. The detector is situated opposite the orifice of the BBR, and consists of

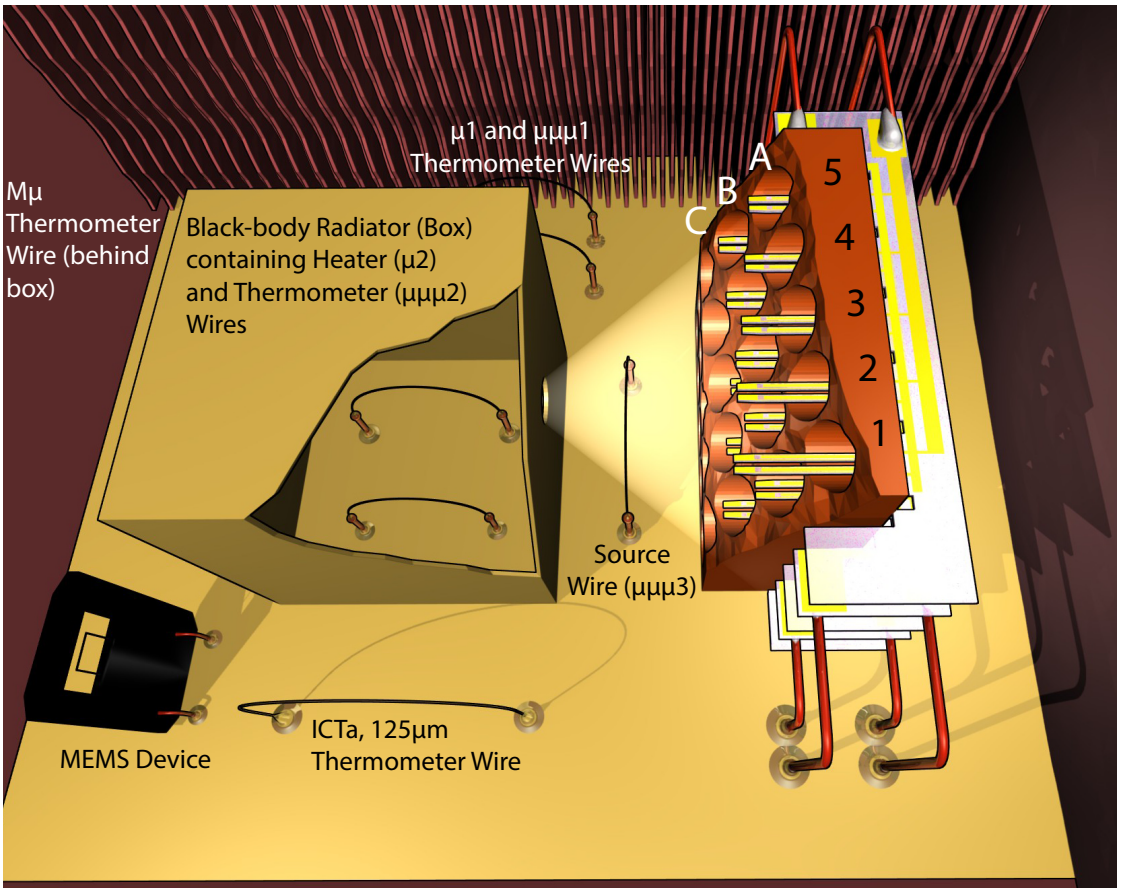

FIGURE 1.1: Render of the experimental cell

a square array of 25 tuning forks, referred to as pixels. The central pixel in the array is designed to be situated level with the orifice of the BBR (in reality the alignment is not perfect, and there is a small offset), the gap between the radiator and the detector is 2 mm. Situated half-way between the radiator and detector is a vibrating wire, called the source wire, the apex of which is designed to be in line with both the BBR orifice and the central pixel (again, in reality there is a small offset). This wire is used to generate a turbulent tangle or a beam of excitations. The remaining vibrating wires are used to monitor the ambient temperature in the cell.

This layout allows us to perform two main types of experiment. First, it allows us to investigate and compare the spatial profile of the excitation beams generated by the BBR and the source wire and extract information about their angular spread. Second, it allows us to measure the spatial variation of the fraction of quasiparticles reflected by the tangle of vortex lines, which we can use to infer information about the spatial variation of the vortex line density, statistical properties of the turbulence and may allow us to investigate large scale structure within the tangle. When a vibrating object, such as a tuning fork, or as is the case here, a vibrating wire, reaches some critical velocity v_c, it begins to emit quasiparticles. For a wire in the bulk superfluid, these excitations are emitted in the form of narrow beams in the direction of motion of the apex of the wire. For a wire in a box, such as that inside a BBR, the excitations scatter from the walls until they thermalise and are emitted from an orifice in a beam.

Interestingly and importantly, our measurements have shown that the beam from the BBR exhibits the same angular spread at all applied powers, details of the characterisation and measurements of the beams are found in chapter 4. This has long been assumed as a property of the beam from a BBR, but is confirmed here for the first time. The turbulence produced by a vibrating object is accompanied by a beam of quasiparticles emitted in the direction of the motion of the object. For a vibrating wire, we find that this beam is of a much lower intensity than the BBR beam and will spread as the velocity of the wire increases.

The profile of the shadow cast by the turbulence generated by a vibrating wire is detailed in chapter 5. We find that the shadow is dominated by reflection in the vicinity of the surface of the vibrating wire and we attribute this to the generation of vortex rings near the surface of the wire. Elsewhere the turbulence appears to be approximately uniform.

We have also studied the fraction of quasiparticles reflected as a function of the velocity of the source wire. This is plotted as the blue line in figure 1.2, for pixel C3. The red line is the force-velocity curve for the source wire, the wire begins to generate turbulence above a critical velocity $v_c \approx 8\text{mms}^{-1}$. The figure reveals information regarding the development of the turbulent tangle. As expected, for velocities below the critical velocity v_c, the reflected fraction is zero, as there are no vortex lines. Above $v/v_c > 1$ the reflected fraction rises rapidly, before plateauing until $v/v_c \sim 2$ where it begins to increase again. There are also some distinctive features in the development of the turbulence, but it is difficult to speculate as to what these represent, these are shown in chapter 6.

We have also measured fluctuations in the quasiparticle shadow caused by fluctuating vortex line density in the tangle to investigate statistical properties of the turbulence. In chapter 7 we find that the power spectrum of the fluctuations exhibits a $f^{-5/3}$ powerlaw, reminiscent of the Kolmogorov spectrum, and consistent with previous measurements [5].

At last we would like to mention that resolution of our measurements approaches limits sufficient to detect a single vortex line in front of the pixel. It can be shown

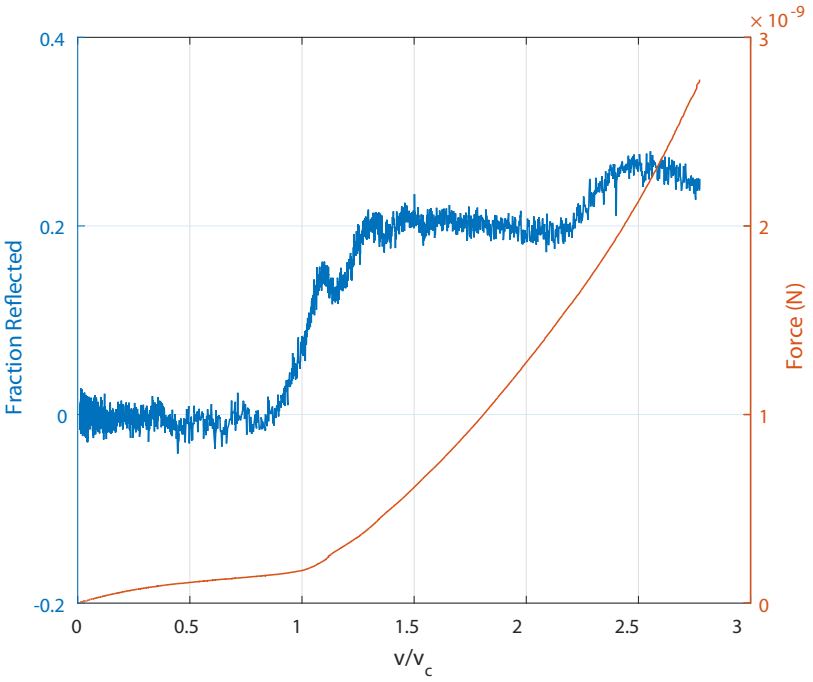

FIGURE 1.2: Plots of the force-velocity profile of the source wire(red) and the fraction reflected in front of pixel C3(blue)

(for example in chapter 7) that a single vortex line pinned across the front of a pixel would result in a 2% reduction in the damping on the tuning fork. The noise level on the tuning forks is such that we can resolve such changes, and opens up the possibility that the detector could be used to investigate single vortex events and coherent structures within the tangle. This is a particularly significant result as it would represent the first device capable of resolving and investigating such structure in the vortex tangle.

In chapter 2 we introduce the core theoretical concepts required to interpret the measurements presented here, in chapter 3 we discuss the measurement techniques used and some of the practical applications of the theory. In chapter 4 we discuss the characterisation of the beams from the BBR and the source wire, in chapter 5 we discuss the shadow cast on the detector by a turbulent tangle generated by the

source wire. In chapter 6 we discuss the development of the shadow cast by the tangle, in chapter 7 we discuss properties of the fluctuations in the line density, and examine the possibility of observing single vortex lines. Finally in chapter, 8 we summarise all findings and postulate how the detector could be refined in the future.

Chapter 2

Theoretical Background

In this chapter we introduce the background theoretical framework required to understand the results presented in this thesis. We will discuss the superfluidity of ^{3}He and compare it to other superfluids. We then will introduce the concept of thermal excitations(quasiparticles) and examine the ballistic limit at very low temperatures, where most of our measurements take place. After, we will discuss the origin of vorticity in quantum fluids, before going on to look at vortex dynamics in ^{3}He.

2.1 Superfluid Helium

The two stable isotopes of helium, ^{3}He and ^{4}He, are unique in nature in that they remain liquid down to absolute zero at zero pressure, due to large zero-point interactions. Both isotopes require pressure of the order of tens of atmospheres to solidify, even in the vicinity of absolute zero. Figure 2.1 [11] shows the pressure-temperature phase diagram of ^{3}He, which clearly illustrates the absence of a triple point. In addition, both isotopes enter superfluid states when cooled below their critical temperature, $T_c = 2.17$ K in ^{4}He (called T_λ for historical reasons [12]), and $T_c = 0.929$ mK in ^{3}He at saturated vapour pressure [13]. Other analogs of superfluids are Cooper Pairs in a superconductor [14], cold atomic gases [15] and, possibly, the core of a neutron star [16].

To understand the superfluidity of ^{3}He it is useful to consider the superfluid state of ^{4}He, which was discovered first and, as a boson, exhibits a simpler mechanism for the formation of the superfluid state. In bosonic systems, there is no Pauli exclusion principle and the maximum occupancy of a single state is unlimited. As a result, below some critical temperature T_B a fraction of the bosons are forced to condense into a common ground state by a mechanism called Bose-Einstein condensation [17]. The superfluidity of ^{4}He is an example of this condensation, though due to interactions between atoms, the real transition temperature $T_\lambda = 2.17$ K is lower than the theoretical $T_B = 3.1$ K [17]. The ground state is perfectly ordered and has zero entropy and viscosity, while the remaining excited bosons are attributed to the normal fluid and possess entropy and viscosity.

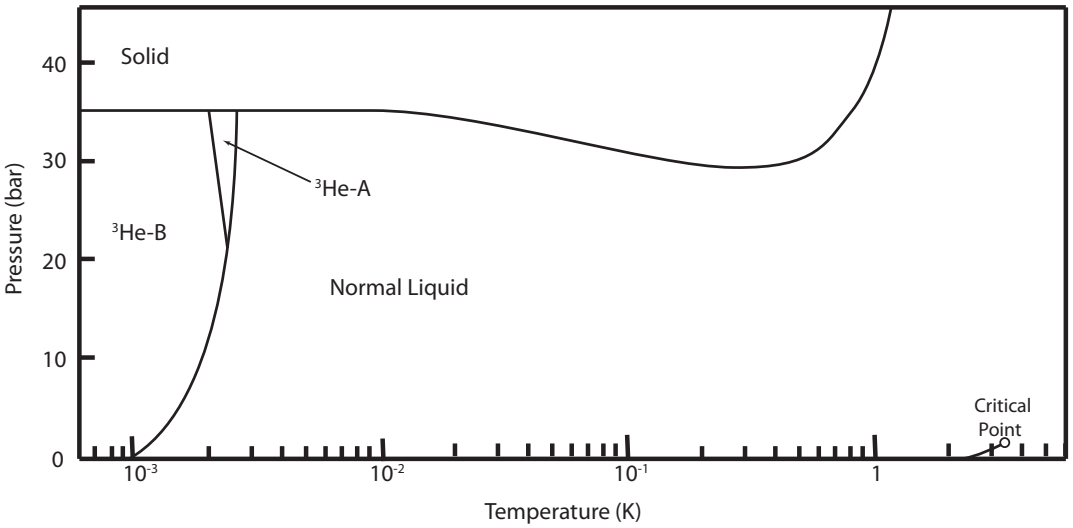

FIGURE 2.1: The phase diagram for ^{3}He in zero applied magnetic field. The critical point is the temperature above which the gas and liquid phases become indistinct and occurs at $T = 5.12$ K.

The ^{3}He atom is a fermion, and is described by Fermi-Dirac statistics, which limits the occupancy of a quantum state to a single atom. The condensation of ^{3}He atoms into a superfluid state is governed by the principles behind the Bardeen-Cooper-Schreiffer(BCS) theory of superconductivity [14]. In the BCS theory an effective attractive interaction between electrons allows them to form pairs, called Cooper pairs, which can be considered composite bosons. The mechanism by which the attraction arises may be summarised as follows: if we imagine an electron moving through a lattice of positively charged metal ions, the motion of the electron will perturb the lattice, due to the attraction between the electron and the ions, another electron travelling through the lattice at later time will feel a greater charge density, resulting in an effective attractive interaction between electrons. In ^{3}He, since atoms carry no net charge, the attractive interaction is a result of the spin

of the ^{3}He atom. When a ^{3}He atom passes through the liquid it will leave a small spin-polarised region in it's wake, which will then be sensed by the spins of other ^{3}He atoms.

Superfluidity in ^{3}He is far more complex than in ^{4}He and supports multiple superfluid phases, figure 2.1 shows that there are two superfluid phases, ^{3}He-A and ^{3}He-B in zero applied magnetic field and only ^{3}He-B will be discussed further here.

2.1.1 ^{3}He-B

The B phase of superfluid ^{3}He is the experimental realisation of the predicted BW-phase by Balian and Werthamer [18]. It contains an equal mixture of all three possible spin projections for the Cooper pair: $|\uparrow\uparrow\rangle, |\uparrow\downarrow\rangle$ and $|\downarrow\downarrow\rangle (S_z = -1, 0, 1)$ and equal mixtures of all three possible projections of the angular momentum $(L_z = -1, 0, 1)$. The simplest combination of these is the state with $J = L + S = 0$. The energy gap in the B-phase is anisotropic in momentum space and has the BCS value of $\Delta = 1.76 k_B T_c$ at low pressure.

In a non-zero magnetic field, the energy gap in the B-phase becomes slightly anisotropic, due to the interactions of the magnetic field with the $|\uparrow\downarrow\rangle$ Cooper pairs. This anisotropy is small in the magnetic fields used in the measurements presented here, so is neglected.

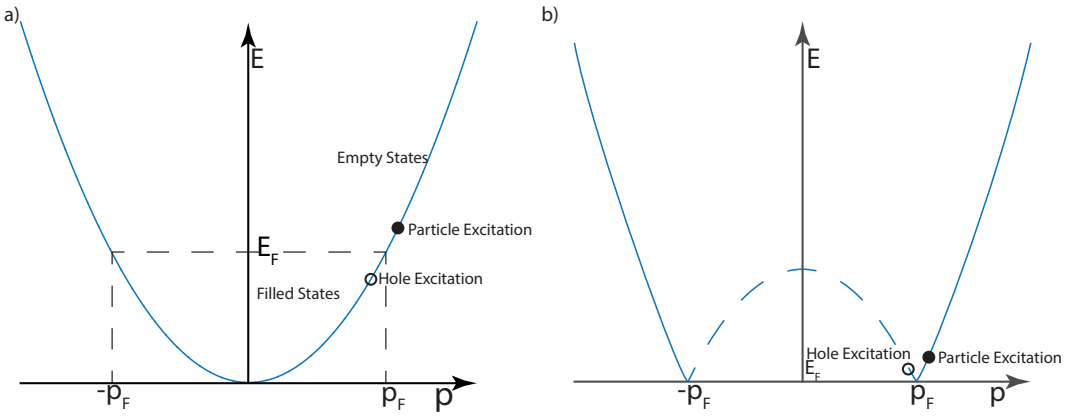

FIGURE 2.2: The dispersion curve for free particles in a Fermi gas: a) the traditional dispersion curve and b) dispersion curve in the excitation picture

2.1.2 The Dispersion Relation and Excitations

The properties of excitations in ^{3}He-B are governed by the dispersion relations. The dispersion relation for free particles has the form $E = p^2/2m$ where p is momentum, m is the mass of a particle and E is energy, and is plotted in figure 2.2a. In a fermionic liquid system which does not exhibit superfluidity, the ground state is one in which all of the one-particle states are filled up to the Fermi energy E_F. An excitation here is formed by giving a particle in the filled state enough energy to move above E_F, leaving a hole in the states below E_F. Fig 2.2a shows the particle and hole excitations as filled and empty circles respectively. Fig 2.2b shows the same process in the so-called excitation picture: the dispersion curve is re-drawn such that the Fermi-energy is now the zero of the energy axis. The particle and hole excitations are now pictured as branches on the dispersion curve. In a normal fermionic excitations can be formed with arbitrarily small energy and

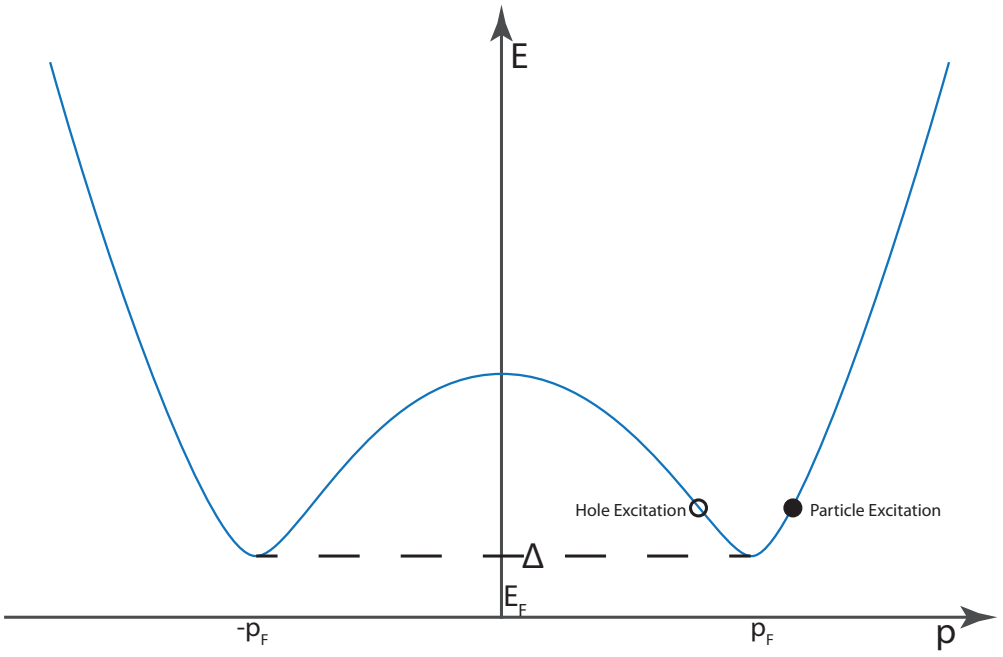

FIGURE 2.3: The dispersion curve for quasiparticles in a Fermionic superfluid with energy gap Δ

momentum.

Figure 2.3 shows the dispersion curve in a system where the pairing interaction leads to a superfluid with an energy gap Δ. The necessity of an energy gap between the ground state and any excited states arises from the ability of the superfluid to flow without breaking the condensate. This was predicted by Landau [19], who introduced the concept of a critical velocity v_L, below which the superfluid will flow without dissipation, and above which the condensate will break down.

It is clear that in this case generation of excitations now requires an energy larger than Δ. It should be noted here that the dispersion curve shown in figure 2.3 is that for a stationary fluid. In the case of a fluid moving with velocity v, the dispersion curve becomes tilted by the Galilean transform $E \rightarrow E + \boldsymbol{p} \cdot \boldsymbol{v}$. When

the velocity is so large that the tilt of the dispersion curve causes it to touch the momentum axis, an excitation will be generated. This occurs at the Landau critical velocity, $v_L = \Delta/p_F$.

The excitations generated by breaking the condensate are quasiparticles and quasiholes and will be referred to as such hereafter. It is common to refer to the overall flux of both quasiparticles and quasiholes simply as the quasiparticle flux, so for the purposes of this thesis, quasiparticle refers to the overall flux of both types of excitation, unless explicitly stated otherwise.

All of the measurements presented in this thesis take place at temperatures below $0.2T_c$. In this regime the mean free path, $l \propto \exp k_B/T$, of the quasiparticles is of the order of a kilometre [12]. The dimensions of the cell we use for this experiment are of the order of centimetres, hence the quasiparticles very rarely interact with each other. For this reason the quasiparticles can be treated as ballistic particles and their dynamics can be calculated from simple kinetics. This is called the ballistic regime.

In this regime the superfluid flow fields affect dispersion curves and hence quasiparticle dynamics. Interaction of quasiparticles with the flow leads to interesting processes like Andreev reflection of quasiparticles that will be described in chapter 3.

2.2 Quantum Turbulence

The key difference between classical and quantum turbulence is that classical vortices may be of any size and carry any amount of circulation, while vortices in a quantum fluid are quantised. They typically carry only one quantum of circulation. This quantisation, in principle, means that the dynamics of systems of quantum turbulence should be simpler than classical turbulence, and that quantum turbulence may act as a model turbulent system. In reality, however, fully developed quantum turbulence is still very complex, and there are still many properties that remain to be explained. Let us first examine turbulence in a classical fluid, before comparing the two systems.

2.2.1 Classical and Quantum Turbulence

The dynamics of a classical viscous fluid can be modelled by the Navier-Stokes equation [20]

$$\frac{\partial \boldsymbol{v}}{\partial t} + (\boldsymbol{v} \cdot \nabla)\boldsymbol{v} = -\frac{1}{\rho}\nabla P + \nu \nabla^2 \boldsymbol{v} \tag{2.1}$$

where $\boldsymbol{v}$ is the velocity of the fluid, P is the pressure, ρ is the density and $\nu = \eta/\rho$ is the kinematic viscosity, η is the viscosity. To characterise the flow of the fluid we introduce a set of dimensionless variables with a characteristic length scale l

and a characteristic velocity u

$$\boldsymbol{r}' = \frac{r}{l}, \boldsymbol{v}' = \frac{\boldsymbol{v}}{u}, t' = \frac{tu}{l}, P' = \frac{P}{\rho u^2}, \nabla' = l\nabla \tag{2.2}$$

In terms of the dimensionless variables, the Navier-Stokes equation becomes

$$\frac{\partial \boldsymbol{v}'}{\partial t'} + (\boldsymbol{v}' \cdot \nabla')\boldsymbol{v}' = -\nabla' P' + \frac{\nu}{ul}\nabla'^2 \boldsymbol{v}' \tag{2.3}$$

The ratio of the inertial (u^2/l) term to the viscous $(u\nu/l^2)$ term determines the characteristics of the fluid flow and is known as the Reynolds number, Re [21]:

$$\mathrm{Re} = \frac{ul}{\nu} \tag{2.4}$$

At Re ≈ 1 the flow is laminar, but as the velocity u increases, and the Reynolds number becomes large(~ 2000) the flow becomes turbulent. The turbulence in classical fluids is very complex with many eddies, and the flow is impossible to predict. Turbulence in quantum fluids is conceptually more simple, due to the quantisation of circulation.

2.2.2 Quantisation of Circulation in a Superfluid

Arguably the most important property of quantum turbulence is the quantisation of circulation that gives it its name. This results from the description of the superfluid phase as a condensate using a macroscopic wave function(order parameter)

$\psi = \psi_0 e^{i\theta}$ where θ is the phase. The circulation around a closed contour dl in a fluid is defined as

$$\kappa = \oint \boldsymbol{v_s} \cdot \boldsymbol{dl} \tag{2.5}$$

The canonical momentum operator is $\hat{p} = -i\hbar\nabla$ and has eigenvalues p, where $\hat{p}\psi = p\psi$. Applying this operator to the superfluid wave function gives

$$-i\hbar\nabla(\psi_0 e^{i\theta}) = p\psi_0 e^{i\theta} \tag{2.6}$$

which leads to

$$\hbar\nabla\theta = p \tag{2.7}$$

The superfluid momentum is $p_s = 2m_3 v_s$, where m_3 is the mass of the ^{3}He atom, hence the superfluid velocity can be written as

$$v_s = \frac{\hbar}{2m_3}\nabla\theta \tag{2.8}$$

the circulation in the superfluid is then

$$\kappa = \frac{\hbar}{2m_3}\oint \nabla\theta \cdot \boldsymbol{dl} \tag{2.9}$$

The phase can only change by integer multiples of 2π around a closed loop. However, in a singly connected volume of superfluid(one in which there is no break in the condensate), any closed loop can be shrunk to a vanishingly small size, hence

the circulation is zero. The finite circulation in the superfluid requires that the volume is multiply connected, in this case the loop cannot be shrunk, and is given by:

$$\kappa = \frac{n2\pi\hbar}{2m_3} = \frac{nh}{2m_3} \tag{2.10}$$

Hence the circulation in superfluid ^{3}He is quantised in units of $h/2m_3$.

Vortex lines can be considered line defects in the fluid, fulfilling the requirement that to observe circulation the volume must be multiply connected. The simplest case is that where the core of the vortex is a region of normal fluid with core radius a_0. Surrounding the vortex core is a region of circulating superflow, where the velocity falls as $1/r$. The circulation at a radius r from a vortex core is $\kappa = 2\pi r v$. Using this along with equation 2.10 allows us to express the superflow velocity at radius r as

$$v = \frac{\hbar}{2m_3 r} \tag{2.11}$$

The vortex core size in ^{3}He-B is of the order of the coherence length in the superfluid, $\xi_0 = 60$ nm at zero pressure [8].

The kinetic energy per unit length of a vortex line is [17]

$$\epsilon_k = \frac{1}{2}\int_{a_0}^{b} 2\pi r \rho v_s^2 dr = \frac{\kappa^2}{4\pi}\rho \int_{a_0}^{b} \frac{1}{r} dr = \frac{\kappa^2}{4\pi}\rho \ln\left(\frac{a_0}{b}\right) \tag{2.12}$$

where the size of the container or inter-vortex spacing $b \gg a_0$. The kinetic energy is proportional to κ^2, hence, two singly-quantised($n = 1$) vortices are energetically favourable to a single double-quantum($n = 2$) vortex. It is clear from this that

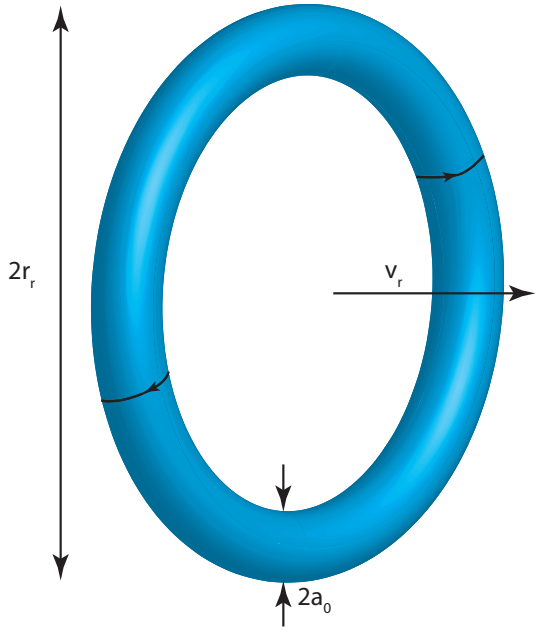

FIGURE 2.4: Diagram of a vortex ring

singly quantised vortices are the favourable vortex line configuration, as double-quantum and higher vortices are unstable and will decay into single-quantum vortices over time. In ^{3}He-B there are two main types of vortices [22]. At high pressure the vortex core consists of circulating normal fluid, as is the case in ^{4}He. At low temperature and pressure the most common vortex is a bound state of two half-quantum vortices [23]. Other, more exotic vortices are possible, such as the spin-mass vortex described in [24].

It is unclear what the mechanism for the nucleation of vortex lines in superfluids is, it is typically assumed that it is due to the stretching of remnant vortices [25]. Remnant vortices are those that remain pinned to surface extrusions from previous turbulent flows [26]. It has also been postulated that nucleation can occur via the resolution of phase-slippage [27, 28]. As topological defects, vortex lines cannot

terminate with a free end in the fluid. Both ends must be pinned, for example to protrusions on objects in the fluid or walls, or to themselves to form a closed loop, as is the case with vortex rings. Vortex rings, an example of which is shown in figure 2.4, are one of the more simple vortex structures. They are typically formed at velocities near some critical velocity by vibrating grids [25] and vibrating wires [29]. Vortex rings propagate under the influence of their own flow field with a velocity given by

$$v_r = \frac{\kappa}{4\pi r}\left(\ln\left(\frac{8r_r}{a_0}\right) - \beta_r\right). \tag{2.13}$$

where r_r is the radius of the ring and β_r is a constant related to the core structure of the vortex.

When two vortex rings or vortex lines approach within some critical distance l of each other, their flow fields perturb each other, this results in a discontinuity in the flow field, which is resolved by the two lines reconnecting to form either new vortex lines or vortex rings [26]. An example of the reconnection of two vortex lines is shown in figure 2.5 [26]. This will eventually to lead to the formation of a random tangle of vortex lines. The key properties of the vortex tangle, when considering the interaction with quasiparticles, are the intervortex spacing, which will determine the distance of closest approach of a quasiparticle to a vortex line, and the line density - the total vortex line length per unit volume. This will be further discussed in chapter 5, when considering the interaction of a quasiparticle with the flow field of a vortex.

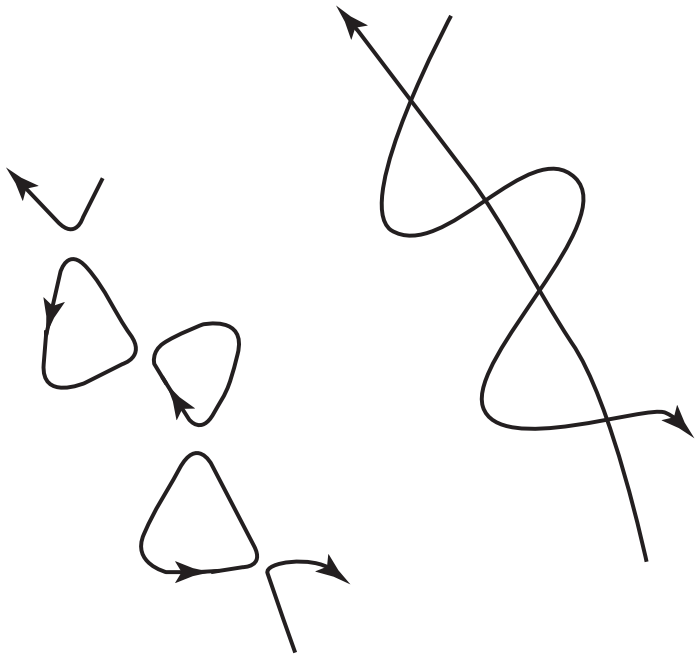

FIGURE 2.5: Example of a reconnection between two vortex lines

2.2.3 Dissipation of Turbulence

Classical turbulence decays by means of an energy cascade, called the Richardson cascade. Energy is injected at large length scales, and is transmitted through eddies to smaller and smaller length scales. When the flow reaches Re ≈ 1 the remaining energy is dissipated through the fluid viscosity. This cascade has a characteristic energy spectrum given by the Kolmogorov law [30].

$$E(k) = C\epsilon^{2/3}k^{-5/3} \tag{2.14}$$

where C is the Kolmogorov constant, ϵ is the rate of energy dissipation and k is the wavenumber. The Kolmogorov spectrum has been confirmed numerically and

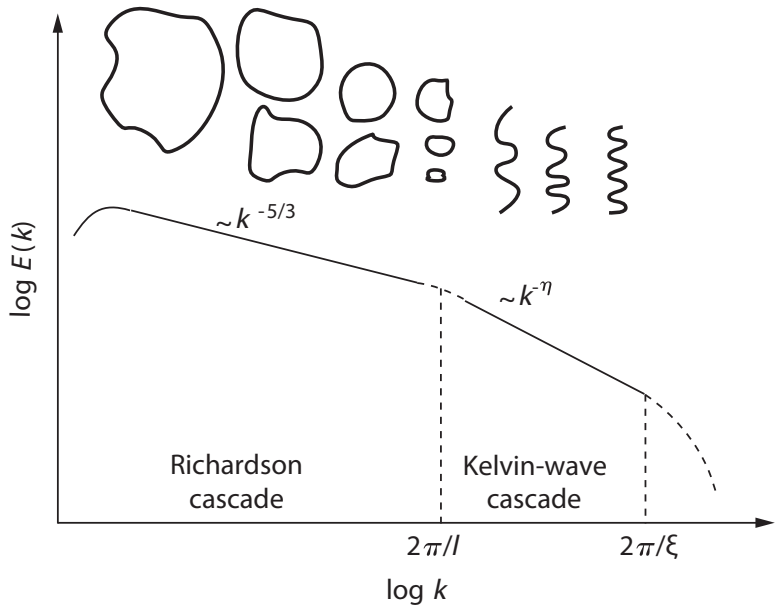

FIGURE 2.6: Schematic of the Energy Spectrum for Quantum Turbulence

experimentally [31] in classical turbulence. The Kolmogorov spectrum however, assumes that the turbulence is isotropic and homogeneous, which is not necessarily the case in real systems. This leads to deviation from the Kolmogorov spectrum which is a phenomenon known as intermittency [31].

The energy spectrum for quantum turbulence is shown in figure 2.6. In quantum turbulence, at large length scales, the situation is similar to that in classical turbulence and a Richardson cascade with associated Kolmogorov spectrum dominates the decay of the turbulence. At intermediate length scales energy is dissipated via a Kelvin-wave cascade [32]. Kelvin waves are helical excitations on the vortex lines, and interaction between Kelvin waves of different wave number becomes the dominant mechanism for the transfer of energy. Below some critical length scale the energy will be dissipated through acoustic phonon emission in ^{4}He [33] or by

quasiparticle emission in ^{3}He [34]. A Kolmogorov-like spectrum has been observed by the direct measurement of the energy dissipated by a turbulence in ^{3}He-B [5].

Chapter 3

Techniques

In this chapter we will discuss the experimental techniques used in the measurements presented in this thesis. We will start by describing the construction of the cell. We then describe the theory behind the motion of vibrating objects in general, before focusing on tuning forks and vibrating wires. We detail the data acquisition techniques. Finally, we discuss the effects of Andreev reflection on vibrating objects, and the behaviour of such devices in superfluid ^{3}He-B.

3.1 Cell Construction

The experimental arrangement was placed in the inner cell of a Lancaster-style nuclear demagnetisation stage [35] which was mounted on the mixing chamber of

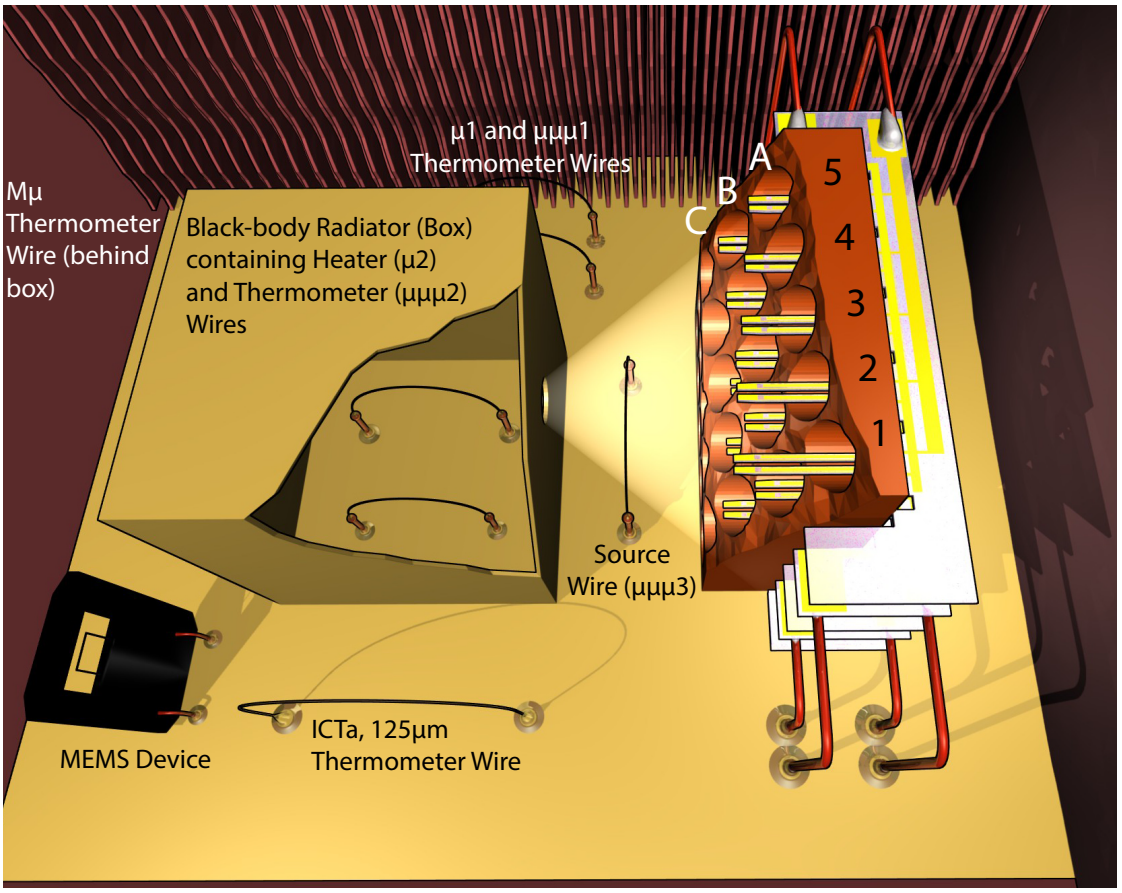

FIGURE 3.1: Render of the experimental cell. Tuning forks are labelled by considering the array as a matrix with the arrays labelled A to E and the forks labelled 1 to 5, hence the central fork is labelled C3. The vibrating wires are labelled according to their diameter.

the Lancaster Advanced Dilution Refrigerator [36]. The inner cell itself is situated in a hollow inside a set of sintered copper plates which act to absorb stray quasiparticle excitations and maintain thermal equilibrium in the cell. The vibrating wires and tuning fork detector are mounted on a base of stycast impregnated paper. Measurements are performed during the slow warm-up following a demagnetisation, during which we achieve temperatures of approximately 100 μK, and provides approximately 5 days of measurement time.

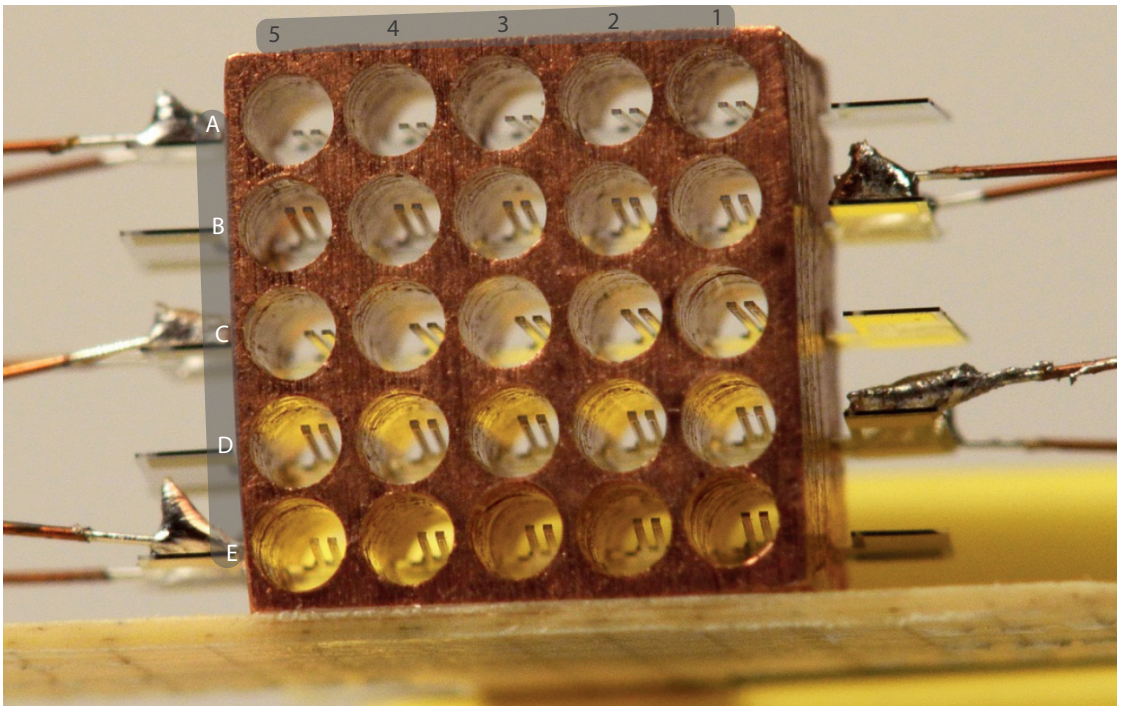

FIGURE 3.2: Photograph of the tuning fork detector

3.2 Cell Construction

The cell layout is reproduced in figure 3.1. The tuning fork detector is a copper block with a face of area 5 mm × 5 mm, a photo of which is shown in figure 3.2. Each tuning fork is situated inside a 1 mm diameter hole in the copper which form the pixels. The tuning forks are mounted from the back of the block in the arrays of 5 forks described earlier. In principle, quasiparticles scatter from the walls of the pixel, ensuring that as many as possible are detected by the tuning fork. However, the back of each pixel is open, so there is some chance that a quasiparticle will travel straight through and not interact with the fork. Geometrical considerations show that this may account for 20% of incident quasiparticles for the central pixels [37].

The black-body radiator is an approximately cubic box made of stycast-impregnated paper with an orifice in one wall. There are two vibrating wires inside, one used for generating thermal excitations - the heater wire, which we call $\mu 2$, and the other used to measure the temperature - the thermometer wire. Excitations generated by the heater wire will thermalise inside the box and be emitted in a beam from the orifice. The thermometer wire allows us to calibrate the temperature of the box against the power applied to the heater wire, allowing the use of the box as a sensitive bolometer [9]. The detector is situated opposite the orifice of the BBR, and consists of a square array of 25 tuning forks, referred to as pixels. The central pixel in the array is designed to be situated level with the orifice of the BBR (in reality the alignment is not perfect, and there is a small offset), the gap between the radiator and the detector is 2 mm. Situated half-way between the radiator and detector is a vibrating wire, called the source wire, the apex of which is designed to be in line with both the BBR orifice and the central pixel (again, in reality there is a small offset). This wire is used to generate a turbulent tangle or a beam of excitations. The remaining vibrating wires are used to monitor the ambient temperature in the cell.

We label the vibrating wires in the cell according to their diameter and function. We call 13.5 μm diameter vibrating wires μ wires, 4.5 μm diameter, $\mu\mu\mu$ wires and the 1.5 μm diameter wire Mμ. $\mu 1$, $\mu\mu\mu 1$ and Mμ are thermometer wires, $\mu 2$ and $\mu\mu\mu 2$ are the heater and thermometer wires in the black-body radiator respectively and $\mu\mu\mu 3$ is the source wire.

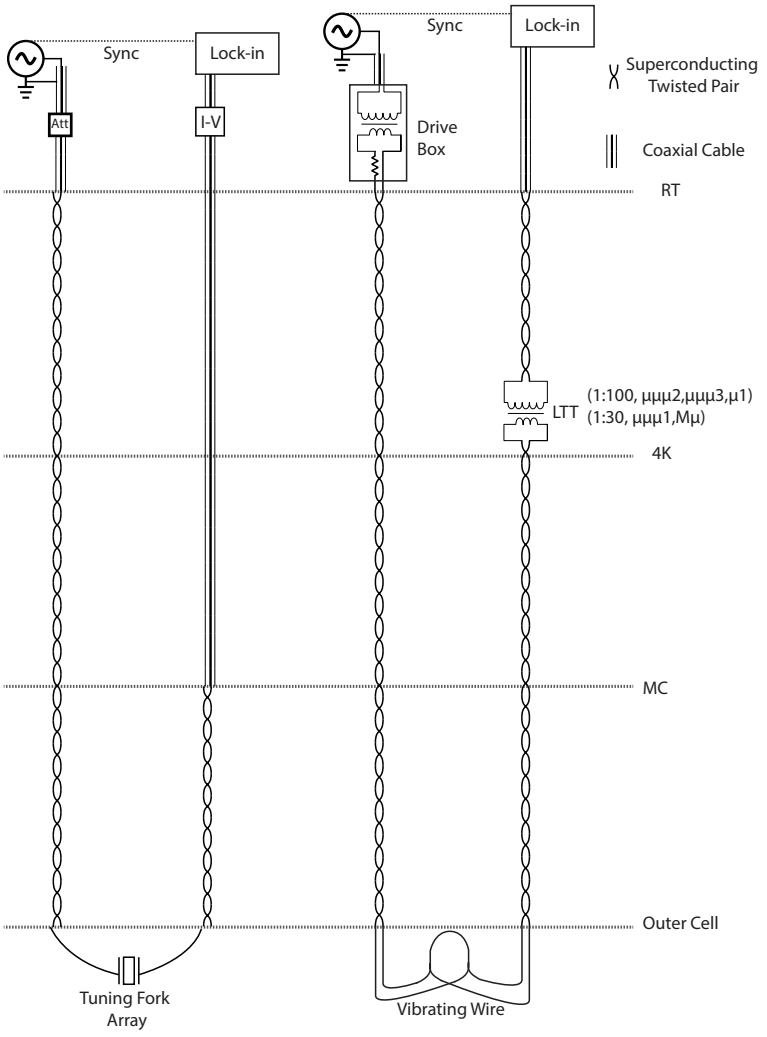

FIGURE 3.3: Wiring Diagram for the Devices in the Cell Left: Tuning fork, Right: Vibrating wire

The electrical measurement scheme for vibrating wires and tuning forks is shown in figure 3.3. The driving signal for the tuning forks is supplied via a twisted pair of wires, which goes from room temperature, is anchored at each stage of the dilution fridge and is connected to the tuning fork leads at the mixing chamber. The response from the tuning forks is connected to superconducting coaxial cables at the mixing chamber and is brought to room temperature via coaxial cable. There are no transformers or attenuators below room temperature in the tuning

fork measurement circuit. In principle it would be best to connect both drive and response of the tuning forks via coaxial cables, but due to space limitations we had to choose one side, and testing indicated that best practice in this case is to connect the response side via coaxial cables. The room temperature measurement scheme for the tuning forks is shown in detail in figure 3.6 and is described in the associated section.

The vibrating wires are connected via superconducting twisted pairs between room temperature and the mixing chamber. Low-temperature transformers are connected on the response side, at 4 K, to increase the small signal output from the vibrating wire. Again, the room temperature measurement scheme will be described alongside the description of the vibrating wires below.

3.3 Vibrating Objects

Vibrating objects such as vibrating spheres [38], vibrating wires [4], vibrating grids [25] and tuning forks [39, 40] are widely used in the study of superfluids. Here, we use tuning forks to detect the flux of thermal quasiparticles and vibrating wires to generate turbulence and quasiparticle beams, and also as thermometers, therefore this discussion will focus on the properties of these devices. Tuning forks were chosen as their resonant frequency can be easily controlled compared to other vibrating devices and they can be manufactured consistently.

3.3.1 Vibrating Object Motion

First we consider the general motion of a vibrating object. A vibrating object in vacuum resonates at a natural frequency ω_0 given by

$$\omega_0 = 2\pi f_0 = \sqrt{\frac{k}{m}} \tag{3.1}$$

Where k is the spring constant and m is the mass of the resonator. Forcing motion with a driving force of the form $F = F_0 e^{i\omega t}$ causes the object to undergo simple harmonic motion with the equation of motion

$$F = m\ddot{x} + m\Lambda\dot{x} + kx \tag{3.2}$$

where x is the displacement, $\dot{x}$ denotes the time derivative of x, hence the velocity, k is the spring constant and Λ is the damping term $\Lambda = i\lambda_1 + \lambda_2$. λ_1 represents the damping due to the inertia of the backflow of the fluid and λ_2 represents the damping due to the dissipative part of the force. Using a trial solution of the form $x = x_0 e^{i\omega t}$ and noting that, for this solution, $x = \dot{x}/i\omega$ gives the force per unit mass:

$$\frac{F}{m} = i\omega\dot{x} + \lambda_2\dot{x} + i\lambda_1\dot{x} - i\frac{k}{\omega m}\dot{x} \tag{3.3}$$

This can be rearranged to give the velocity $\dot{x}$

$$\dot{x} = \frac{F}{m}\frac{\lambda_2\omega^2 + i\omega(\omega_0^2 - \omega^2 - \omega\lambda_1)}{\lambda_2^2\omega^2 + (\omega_0^2 - \omega^2 - \omega\lambda_1)} \tag{3.4}$$

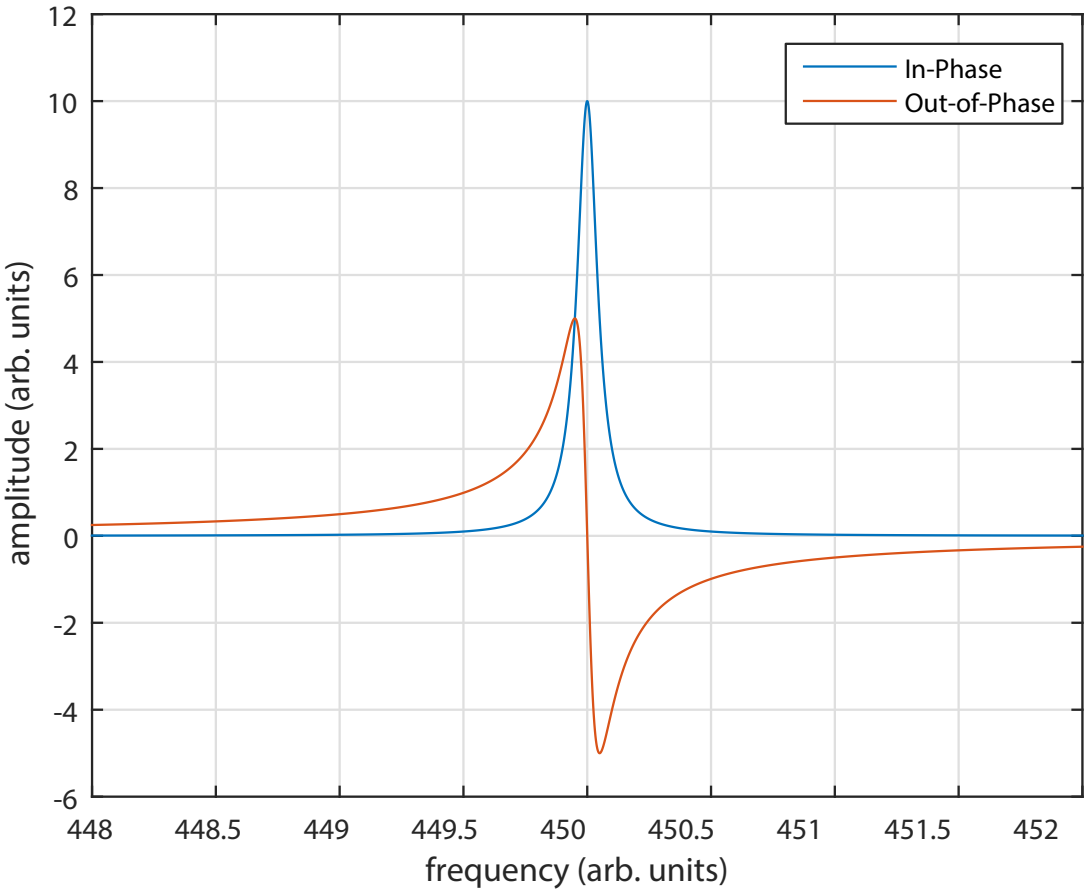

FIGURE 3.4: Ideal Lorentzian in-phase and out-of-phase resonator responses

This has real and imaginary parts $\Re(\dot{x})$ and $\Im(\dot{x})$ respectively:

$$\Re(\dot{x}) = \frac{F}{m} \frac{\lambda_2 \omega^2}{\lambda_2^2 \omega^2 + (\omega_0^2 - \omega^2 - \omega\lambda_1)} \tag{3.5}$$

$$\Im(\dot{x}) = \frac{F}{m} \frac{\omega(\omega_0^2 - \omega^2 - \omega\lambda_1)}{\lambda_2^2 \omega^2 + (\omega_0^2 - \omega^2 - \omega\lambda_1)} \tag{3.6}$$

The real part of the velocity is the velocity in phase with the driving force and the imaginary part the out-of-phase component, these components are plotted in figure 3.4. The condition for resonance is that $\Re(\dot{x})$ is maximised when $\Im(\dot{x}) = 0$

at $\omega = \omega_0$. $\Re(\dot{x})$ is maximised when $(\omega_0^2 - \omega^2 - \omega\lambda_1)^2 = 0$ and:

$$\Re(\dot{x})_{max} = \frac{F}{m}\frac{1}{\lambda_2} \tag{3.7}$$

a consequence of this is:

$$\omega_0^2 - \omega^2 - \lambda_1\omega = 0 \tag{3.8}$$

Completing the square here gives

$$(\omega_0 - \omega)(\omega_0 + \omega) - \omega\lambda_1 = 0 \tag{3.9}$$

$$\omega_0 - \omega = \frac{\omega\lambda_1}{\omega_0 + \omega} \tag{3.10}$$

for small shifts such that $\omega_0 \approx \omega$

$$\Delta\omega_1 = \omega_0 - \omega = \frac{\lambda_1}{2} \tag{3.11}$$

where $\Delta\omega_1$ is the shift of the resonance from it's vacuum value.

The width, $\Delta\omega_2$, which is defined as the width of the resonance at half of its maximum height, can be found by considering the relevant conditions. The condition for half-height is that $\Re(\dot{x}) = \Re(\dot{x})_{max}/2$ at $\omega = \omega_{1/2}$ which leads to

$$\frac{\lambda_2\omega_{1/2}}{\lambda_2^2\omega_{1/2}^2 + (\omega_0^2 - \omega_{1/2}^2 - \omega_{1/2}\lambda_1)^2} = \frac{1}{2\lambda_2} \tag{3.12}$$

This requires that $(\omega_0^2 - \omega_{1/2}^2 - \omega_{1/2}\lambda_1)^2 = (\lambda_2\omega_{1/2})^2$ results in

$$(\omega_0 - \omega_{1/2}) = \frac{\omega_{1/2}(\lambda_1 \pm \lambda_2)}{\omega_0 + \omega_{1/2}} \tag{3.13}$$

We assume that $\omega_0 \approx \omega_{1/2}$, then

$$(\omega_0 - \omega_{1/2}^{\pm}) = \frac{\lambda_1 \pm \lambda_2}{2} \tag{3.14}$$

which gives the width $\Delta\omega_2$ as

$$2\pi\Delta f_2 = \Delta\omega_2 = \omega_{1/2}^{+} - \omega_{1/2}^{-} = \lambda_2 \tag{3.15}$$

Using equations 3.7 and 3.15 together results in a useful quantity called the height-times-width-over-drive(HWD).

$$HWD = \frac{v_0\Delta f_2}{F} = \frac{1}{2\pi m} \tag{3.16}$$

3.3.2 Tuning Forks

Quartz tuning forks(QTFs) are piezo-electric resonators, used as a 32 kHz frequency standard for timing circuits and for distance control in scanning probe microscopy [41]. More recently, tuning forks have seen increasing use as probes for various properties of quantum fluids [39, 42–44]. They are particularly useful as

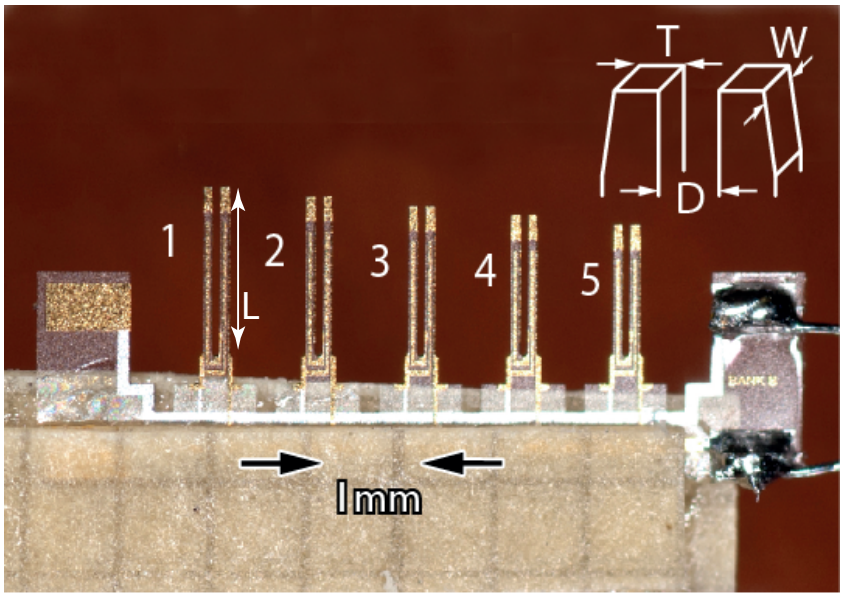

FIGURE 3.5: Photo of an array of quartz tuning forks, showing the key dimensions, the inset shows the key dimensions of the tuning fork, which are defined in the text.

their properties are quite easily controlled, hence specific resonant frequencies and device sizes can be chosen. In the case of the measurements made in this thesis, the tuning forks are custom-designed, and manufactured by Statek Corp. [45]. The three key dimensions that can be used to control the properties of the tuning forks are the tine length, $\mathcal{L}$, the tine width, $\mathcal{W}$, and the tine thickness $\mathcal{T}$, shown in figure 3.5, the spacing between tines, $\mathcal{D}$ is also shown in this figure.

Tuning forks are voltage driven, current response resonators. The typical measurement scheme, shown in figure 3.6 consists of a sinusoidal driving signal supplied by an Agilent 33520 waveform generator, which is appropriately attenuated, this attenuation is used to prevent the tuning fork from being overdriven, which would result in a non-linear response from the tuning fork, and in extreme cases could

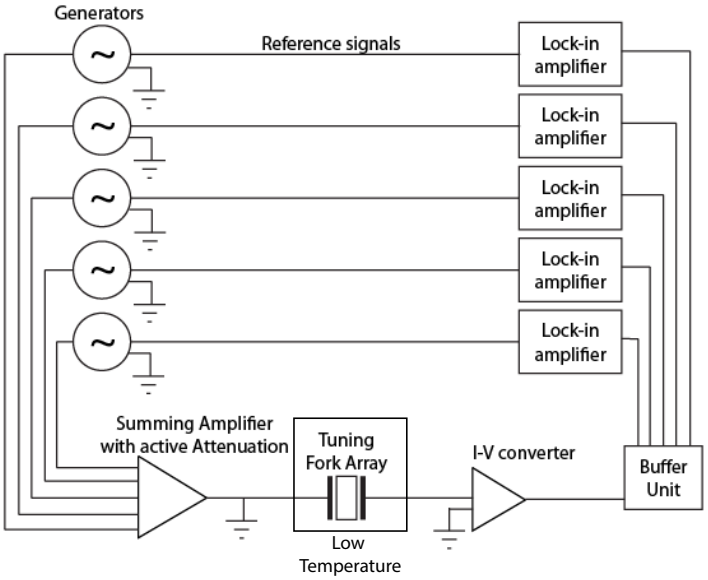

FIGURE 3.6: Measurement circuit for tuning fork arrays. The summing amplifier and buffer unit are custom-made devices that multiplex and demultiplex the five signals respectively. The drive signal is attenuated at the summing amplifier, typically with a factor of 1000.

damage the tines of the tuning fork. The response current, which is typically very small, is converted into a voltage by means of a custom-made high gain($\sim 10^6$V/A), current-to-voltage converter, which is described in [46]. The output voltage is then measured by an SRS SR830 lock-in amplifier.

The response current, I is proportional to the rate of change of the deflection, v of the tuning fork tines.

$$I = av \tag{3.17}$$

The constant of proportionality a is called the fork constant and has a theoretical value [47]

$$a = 3d_{11}E\frac{\mathcal{TW}}{\mathcal{L}} \tag{3.18}$$

where $d_{11} = 2.31 \times 10^{-12}$ m/V is the longitudinal piezo-electric modulus of quartz and $E = 7.87 \times 10^{10}$ N/m^2 is the elastic modulus of quartz. The fork constant can be measured optically using laser vibrometry, however, this technique is not suitable for use at cryogenic temperatures, where the fork constant is determined electrically. Optical and electrical measurements of tuning forks agree within 10% [48]. The driving force applied to the fork is

$$F = \frac{aV}{2} \tag{3.19}$$

where V is the driving voltage. The fork constant by this method is given by

$$a = \sqrt{\frac{2m\Delta\omega I_0}{V_0}} \tag{3.20}$$

where $m = 0.25\rho_q\mathcal{LTW}$ is the effective mass of a tine, $\rho_q = 2659$ kg/m^3 is the density of quartz, $\Delta\omega$ is the frequency width, I_0 is the current amplitude at resonance, and V_0 is the associated driving voltage amplitude. This equation can be obtained from equation 3.16 for the HWD along with equations 3.17 and 3.19. This typically gives about 30% deviation from the theoretical value.

In the case of the measurements presented here, the forks are manufactured in arrays, shown in figure 3.5, each containing five forks. The forks in the array are connected in parallel and share a common pair of leads for drive and response. An operational amplifier circuit with a gain of 1 is used to combine drive signals from five waveform generators, this combined signal is then used to drive the all of the

forks on an array. Each waveform generator is referenced to a lock-in amplifier, and in this way the individual forks can be measured. The arrays used here are designed such that the 25 forks span a range of 20 to 40 kHz. On a single array the resonant frequencies have a spacing of 3 kHz and the arrays are chosen such that there is no overlap and minimal chance of cross-talk between tuning forks. Characterisation of the arrays in vacuum and in ^{4}He is described in [37].

The tines of the tuning forks can be modelled as cantilevered beams [49]. The electrodes on the forks are patterned such that the strongest coupling is to the flexure modes of the tines, and, in vacuum, flexure modes up to the 4th mode can be measured for forks of the type described here (in helium large damping at high frequency prevents measurement of modes above the first or second) [50].

3.3.3 Vibrating Wire Resonators

The vibrating wire resonators(VWRs) used in this cell are all single-filament semi-circular loops, most made from Niobium-Titanium(NbTi) and one from Tantalum(Ta). The NbTi wires are made by bending a length of multi-filamentary wire into a semi-circle, then etching away the cladding, and cutting the filaments until a single one remains. The Ta wire is simply formed from a Ta wire bent into a semi-circular shape.

The wire loops are situated in a fixed vertical magnetic field. An AC drive current is supplied to the wire by way of a step-down transformer and load resistance from an arbitrary-waveform signal generator. The time-varying current in a magnetic

field $\boldsymbol{B}$ induces a Lorentz force on the wire, which causes it to vibrate at the frequency of the driving signal. The velocity and amplitude of the vibrations are maximised at the resonant frequency of the oscillator.

Motion of the current-carrying wire in the magnetic field induces a voltage according to Faraday's law:

$$V = -\frac{d(\boldsymbol{B} \cdot \boldsymbol{A})}{dt} \tag{3.21}$$

Where $\boldsymbol{A}$ is the vector area bound by the wire. For a goal-post shaped vibrating wire of leg-spacing D, with cross-bar perpendicular to the magnetic field the Lorentz force on the crossbar is

$$F = CBID \tag{3.22}$$

where C is a constant of order unity which accounts for the shape of the wire and I is the current. The Faraday voltage V induced due to the motion of the cross-bar in the magnetic field is

$$V = BD\dot{x} \tag{3.23}$$

For a rigid semi-circular wire loop the area bounded by the loop is $\pi D^2/8$ and the rate of change of the angle which it makes to the field is $2\dot{x}/D$, so the velocity of the apex of the wire loop is

$$\dot{x}_0 = K\frac{V_0}{BD} \tag{3.24}$$

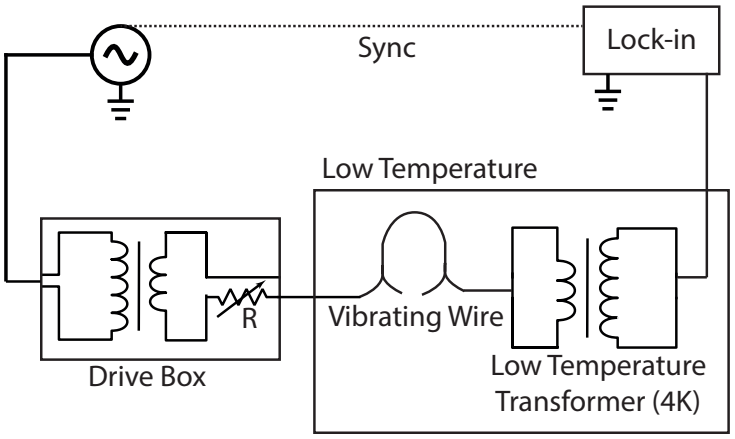

FIGURE 3.7: Measurement circuit for vibrating wires. The drive box contains a step-down transformer and a variable load resistor R. The box labelled low temperature shows the devices that are kept at low temperature.

where $K = 4/\pi$ is a constant for a semi-circular wire [51] and $\dot{x}_0$ and V_0 are the velocity and Faraday voltage at resonance respectively.

Using equations 3.24 and 3.16, we can express the HWD of a vibrating wire as

$$\frac{\Delta f_2 V_0}{I_0} = \frac{C}{K}\frac{B^2 D^2}{2\pi m}. \tag{3.25}$$

So the HWD of a given vibrating wire depends only on the magnetic field B, and can be used to ensure that the wire behaves as expected when the field is changed.

The vibrating wires are driven by supplying a signal from an Agilent 33250 signal generator to a step-down transformer, typically of a 6 : 1 ratio. This signal is then converted to a current and further stepped down by a load resistor. The Faraday voltage response from the wire is stepped up using a low-temperature transformer at 4 K, the in-phase component V_x and out-of-phase component V_y are then measured using an SRS SR830 lock-in amplifier. The measurement circuit

is shown in figure 3.7.

3.4 Data Acquisition Techniques

3.4.1 Frequency Sweep

To determine the Lorentzian width(Δf_2) of the resonance of vibrating devices we use a frequency sweep. We measure frequency sweeps by driving the device at some constant drive V_{exc} and sweeping through a range of frequencies near the resonance. The in-phase voltage V_x and the out-of-phase voltage V_y are constantly monitored and related to the in-phase and out-of-phase components of the velocity respectively.

The frequency sweep can be used to calibrate the phase correction (if any) required due to some small phase angle θ between the in-phase and out-of-phase voltages. We can also use the frequency sweep to determine the height-times-width-over-drive(HWD) value, which for tuning forks is constant, and can be related to the fork constant, a, and for vibrating wires depends only on the magnetic field.

At very low temperatures, the width reduces to values of the order of 10^{-2} Hz hence care must be taken to perform frequency sweeps such that the data acquisition rate is slower than the mechanical time constant $\tau = 1/\pi\Delta f_2$. Failing to do this results in ringing if the acquisition rate is much quicker than τ, or misshapen Lorentzian curves if the rate is slightly quicker than τ. In practice this means that at the

lowest temperatures we measured frequency sweeps with 10^{-4} Hz frequency steps and held at each point for 36 s.

3.4.2 Amplitude Sweep

Amplitude sweeps are performed by ramping the driving force whilst holding the device at it's resonant frequency. This is done by setting the desired driving force and varying the frequency until the quantity V_y/V_x falls below some threshold value, typically 1%. In practice there will be some background in both the in-phase and out-of-phase voltages, which must be subtracted before attempting to find the resonant frequency.

The background voltages can be characterised by using the same method as an amplitude sweep, but at some constant frequency chosen sufficiently far from resonance that no component of the resonance affects the measurement. This is done symmetrically around the resonance, and the value of the background at the resonant frequency is taken to be the average of the two measurements. This gives some intercept a_0 which is the background at zero drive, and a slope a_1, which when multiplied by the drive, gives the drive-dependent background.

Again, care must be taken so that the rate of the frequency variation is not faster than the mechanical time constant of the tuning fork.

3.4.3 Tracking

The majority of our measurements rely on tracking a large number of devices at their resonant frequency, using the signal height and HWD to recover the width. This is typically done by setting some required signal height, and using a software based feedback loop to control the frequency and driving force such that the background-corrected out-of-phase voltage is minimised.

3.5 Damping on a Paddle in ^{3}He-B

The damping on a vibrating object at low velocities in superfluid ^{3}He-B is dominated by interactions with thermal quasiparticles. The force exerted on the object can be calculated by considering the interactions of the gas of thermal quasiparticles with the flow field surrounding an infinite vibrating paddle. Here we consider the paddle as the general case, and assume that it can be applied to the face of the tuning fork and the loop of the vibrating wire.

We begin by considering the case of a classical gas of particles with momentum p_F and group velocity v_g. From kinetic theory the force exerted on a wall by the gas is [20]

$$F = p_F A n v_g. \tag{3.26}$$

Where n is the number of particles per unit volume and A is the area of wall under consideration. For an infinite paddle moving at a velocity v in the gas, the

resultant force is the difference between the force on the front and back of the paddle, which is

$$F = 2Ap_F nv. \tag{3.27}$$

In superfluid ^{3}He, however, the situation is slightly different. We consider the gas of thermal excitations, which is comprised of particles and holes. The holes have negative effective mass, and hence, the momentum transfer with the paddle is in the opposite sense compared to particles. If the momentum of holes and particles were identical (but opposite), this would then result in cancellation of the forces exerted by each and there would be no net force on the paddle, which would result in zero thermal damping on a vibrating object in superfluid ^{3}He. Clearly this is not the case in reality, and it turns out there is some very small asymmetry between the particle and hole momenta, and quasiparticles and holes interact with flow fields in different ways.

We can derive the damping force on a paddle in the superfluid by considering the forces exerted in four cases, for holes and particles hitting either side of the particle, this is shown in figure 3.8. We first consider a quasiparticle at position 1) in figure 3.9. This quasiparticle has no available states to propagate into at the paddle surface, so is Andreev-reflected and retraces it's path. A fraction f_T of quasiparticles will traverse the flow and reach the paddle surface. A quasihole approaching from position 2) in figure 3.9 is able to freely traverse the flow, and all such quasiholes will reach the surface of the paddle. The forces, F_1 due to quasiholes and F_2 due to quasiparticles hitting the front of the paddle are then,

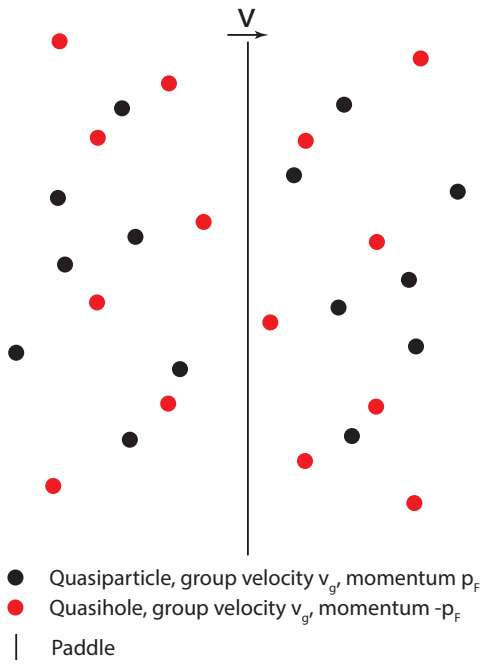

FIGURE 3.8: Schematic showing the interaction of a gas of quasiparticles with a moving paddle in ^{3}He-B

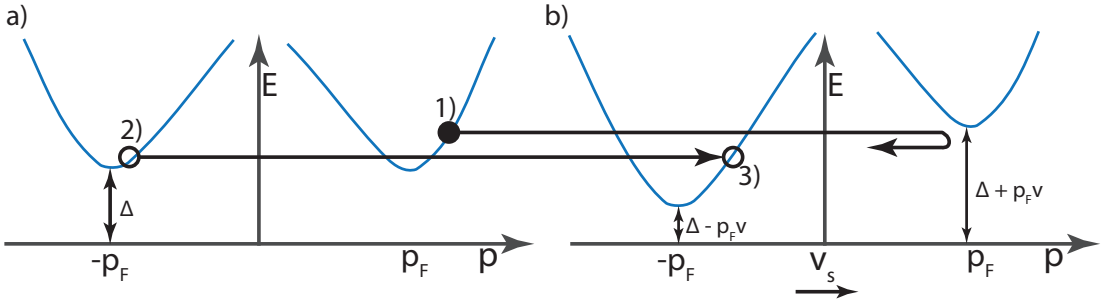

FIGURE 3.9: Dispersion curves at a) a large distance from the paddle surface and b) at the paddle surface

note that the group velocity $v_g \sim 50$ ms^{-1} is much greater than the velocity of the paddle, v:

$$F_1 = An(v_g)p_F \tag{3.28}$$

$$F_2 = -Anv_g p_F f_T \tag{3.29}$$

At the back of the paddle, the situation is reversed, with quasiparticles being able

to freely traverse the flow and some fraction f_T of the quasiholes reaching the paddle surface, hence the forces, F_3 due to quasiholes and F_4 due to quasiparticles hitting the back of the paddle are

$$F_3 = -Anv_g p_F f_T \tag{3.30}$$

$$F_4 = Anv_g p_F \tag{3.31}$$

The total force on the paddle is then

$$F_{TOT} = 2Anv_g p_F (1 - f_T) \tag{3.32}$$

The total excitation flux incident on the paddle $\langle nv_g \rangle_i$ is given by the integral

$$\langle nv_g \rangle_i = \int_{\Delta}^{\infty} f(E)g(E)v_g(E)dE \tag{3.33}$$

where $f(E)$ is the Fermi-Dirac distribution function, in the low temperature limit we need only consider excitations within $k_B T$ of the energy gap, in this case we can replace the distribution function with that for Maxwell-Boltzmann statistics: $f(E) = \exp -E/k_B T$, $g(E)$ is the density of states and v_g is the group velocity. Solving the integral in equation 3.33 gives:

$$\langle nv_g \rangle_i = g(E_F)v_F k_B T \exp\left(\frac{-\Delta}{k_B T}\right) \tag{3.34}$$

where $g(E_F)$ is the density of states at the Fermi energy and v_F is the Fermi velocity. The fraction of excitations f_T capable of traversing a flow field of velocity v can be calculated by considering the flux of excitations that can overcome the potential barrier presented by the flow field. The flow presents a barrier of $p_F v$ to the excitations, hence the lower limit in the integral in equation 3.33 becomes $\Delta + p_F v$ and the transmitted excitation flux, $\langle n v_g \rangle_t$ is:

$$\langle n v_g \rangle_t = g(E_F) v_F k_B T \exp\left(\frac{-(\Delta + p_F v)}{k_B T}\right) \tag{3.35}$$

so the fraction transmitted is

$$f_T = \frac{\langle n v_g \rangle_t}{\langle n v_g \rangle_i} = \exp\left(\frac{-p_F v}{k_B T}\right) \tag{3.36}$$

The damping force becomes

$$F = 2A\langle n v_g \rangle p_F \left[1 - \exp\left(\frac{-p_F v}{k_B T}\right)\right] \tag{3.37}$$

This is the damping on an infinite paddle in one dimension. This then has to be generalised to three dimensions in the following way [52]:

$$F_{Th} = 2\gamma L d \langle n v_g \rangle p_F \left[1 - \exp\left(\frac{-\lambda p_F v}{k_B T}\right)\right] \tag{3.38}$$

where λ and γ are geometrical factors of order unity. γ accounts for roughness of the surface of the wire and the actual shape of the object in question and λ

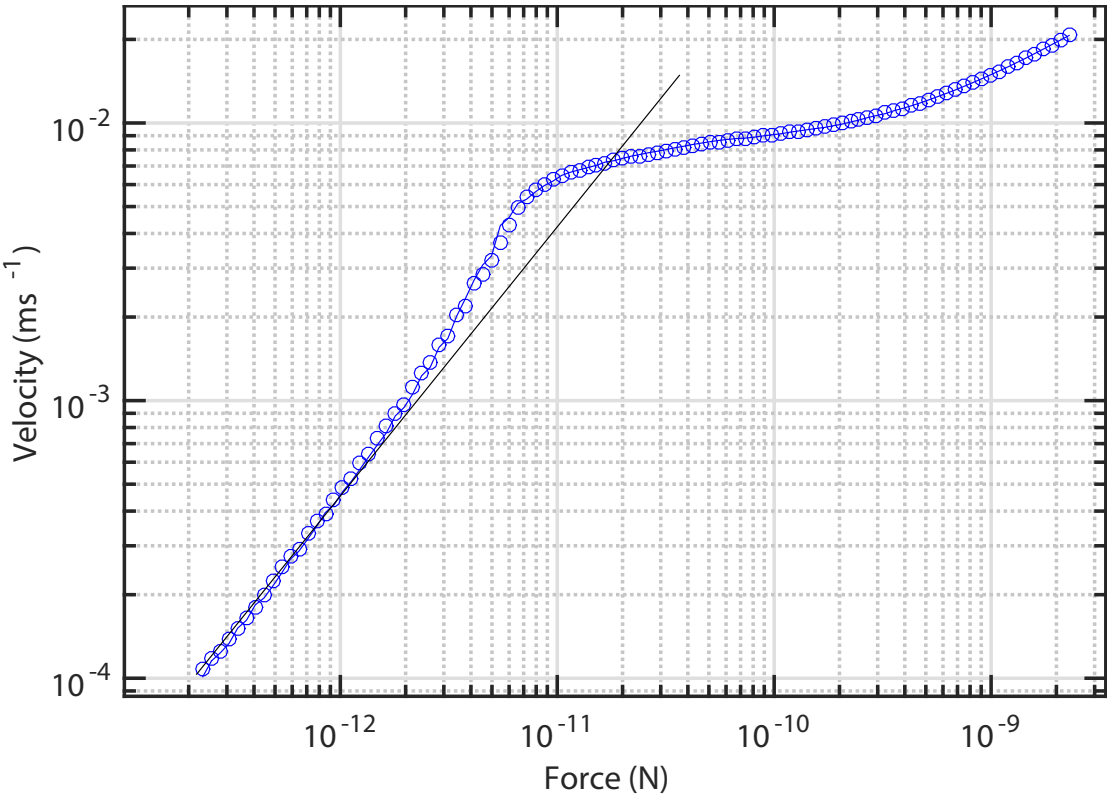

FIGURE 3.10: Force-Velocity Profile for the Source Wire. The solid line is a guide of slope unity

accounts for averaging over multiple dispersion curves in three dimensions. The subscript Th has been added to indicate that this is the damping force due to thermal quasiparticles.

3.6 Thermal Force on a Vibrating Wire

Figure 3.10 shows the force-velocity curve for the source wire. The total damping force can be written as

$$F = F_0 + F_{Th} + F_{ex} \tag{3.39}$$

Where F_0 is the temperature independent intrinsic contribution, F_{Th} is the thermal damping and F_{ex} accounts for any excess damping due to pair-breaking and turbulence.

In the low velocity limit the thermal damping force reduces to:

$$F_{v\to 0} = 2\gamma L d\langle n v_g\rangle \frac{\lambda p_F v}{k_B T} \tag{3.40}$$

using this along with equation 3.16 and recalling $\langle n v_g\rangle = g(p_F) k_B T \exp\left(-\Delta/k_B T\right)$ means we can express the linewidth of the resonance due to thermal damping as

$$\Delta f_2 = \frac{\gamma' d p_F^2 g(p_F)}{\pi m} \exp\left(\frac{-\Delta}{k_B T}\right) \tag{3.41}$$

Where we have collected all constants in equation 3.40 into a single constant called γ'. This corresponds to the linear part in figure 3.10 where the force is proportional to the velocity, and the damping Δf_2 is constant. This indicates the flow around the wire is laminar. At low temperatures this regime is dominated by the temperature-independent intrinsic damping, but as the temperature increases the thermal damping begins to dominate.

3.7 Non-Linear Damping

As the velocity approaches the pair-breaking critical velocity $v_c \sim 8$ mms^{-1} the force velocity curve deviates from the laminar slope. This appears in our measurements as a velocity enhancement in drive sweeps, or as a decrease in width as the required signal height is increased whilst tracking. This is known as non-linear damping, and results from the Andreev-reflection of excitations by the flow field around the wire. For direct comparison it is important that we can recover the width of the device as if it continued along the laminar slope, we call this process non-linear correction or linearisation.

The damping due to thermal quasiparticles on a vibrating object is

$$\Delta f_2^{Th} = \Delta f_2^M - \Delta f_2^0 \tag{3.42}$$

where Δf_2^M is the total measured damping and Δf_2^0 is the intrinsic mechanical damping. The linear damping can be recovered from the non-linear damping by normalising the general thermal damping force (equation 3.38) by the damping force in the low velocity limit (equation 3.40):

$$\frac{F_T}{F_{v\to 0}} = \frac{k_B T}{\lambda p_F v}\left[1 - \exp\left(\frac{-\lambda p_F v}{k_B T}\right)\right] \tag{3.43}$$

Then the linearised width is given by

$$\Delta f_2^T = (\Delta f_2^M - \Delta f_2^0)\frac{\lambda p_F v}{k_B T}\left[1 - exp\left(\frac{\lambda p_F v}{k_B T}\right)\right]^{-1} \tag{3.44}$$

where Δf_2^T is the true (corrected) thermal damping, Δf_2^M is the measured total damping, and Δf_2^0 is the intrinsic mechanical damping of the device. λ is a constant of order unity, which is a characteristic of a given device. Equation 3.44 can be used to find the value of λ.

The value of λ for a vibrating object is determined by measuring the linewidth as the velocity is increased towards the pair-breaking velocity. The temperature is provided by a remote thermometer driven in it's linear regime. λ is then varied until the linear width from the beginning and end of the measurement is recovered for each velocity-step. We refer to this process as linearisation. In this case we only consider corrections for the tuning forks, as the vibrating wires are driven exclusively in their low-velocity, linear regime during their use as thermometers.

Figure 3.11 shows the typical result of applying the correction to a tuning fork. In this case it is clear that the linearisation does not work well, particularly at higher velocities. At these velocities the width begins to increase, despite the correct linearisation at lower velocities. This has been seen previously for similar tuning forks [52]. In this case it was assumed that flow enhancement around the sharp corners of the tines of the tuning fork was resulting in parts of the fork locally exceeding the pair-breaking critical velocity. Correcting for this can be done by

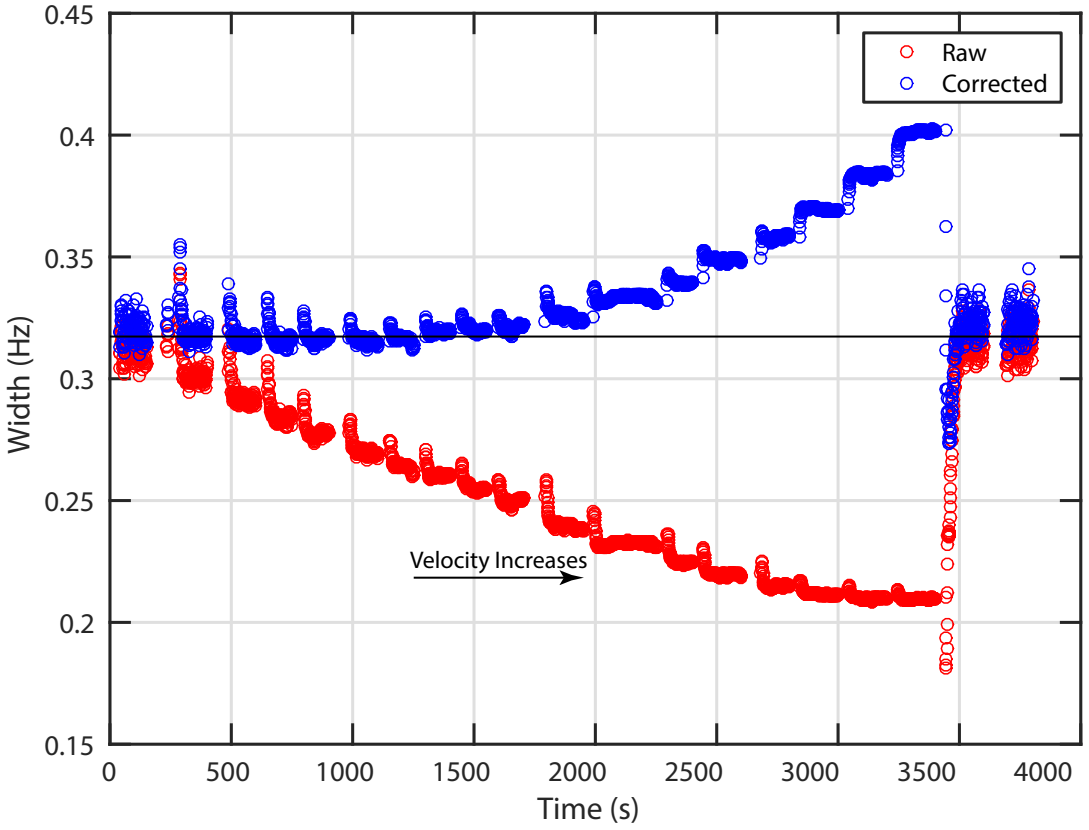

FIGURE 3.11: Plot of the change in width of fork C3 as the velocity is increased (shown by the arrow) in red and the effect of attempting to linearise this data in blue.

measuring the intrinsic damping as a function of the velocity, and then using that in place of the velocity independent intrinsic damping in equation 3.44. The forks that we use in this experiment are more sensitive to thermal quasiparticles, and we have not managed to achieve a temperature low enough to measure a drive sweep of the forks in their intrinsic limit. Hence, here we assume that the correct value of λ for the correction is that which linearises the width at low velocities. Using this assumption, we find that the values of λ for the tuning forks are all approximately 0.65.

3.8 Pair-Breaking and the Generation of Turbulence by a Vibrating Object

Above some critical velocity v_c the vibrating object will begin to break the Cooper pairs in the condensate. This appears as a sharp deviation from the laminar flow as the greater damping due to the pair-breaking dominates. For the vibrating wire shown in figure 3.10, this critical velocity is $v_c \approx 8$ mms^{-1}. This is approximately a factor of three smaller than the Landau critcal velocity $v_L = 27$ mms^{-1} in ^{3}He-B. This phenomena was explained by Lambert [53] and Volovik [54]. For a cylindrical object of radius a moving at velocity v in the superfluid, the maximum value of the superflow velocity is $v_s = 2v$ at the surface of the cylinder. The energy gap is assumed to be completely suppressed at the surface of the wire [55]. This allows quasiparticles to be generated at the surface of the wire at arbitrarily low velocities. However for the damping on the wire to change, these quasiparticles must be able to escape from the wire surface. For the cylindrical wire, the highest energy of a created quasiparticle is $+2p_F v$, the lowest available energy state in the bulk is $\Delta - p_F v$. The quasiparticles can then only escape if the wire exceeds some critical velocity $v_c = v_L/3$. For a more general geometry, the maximum velocity at the surface is $v_s = \alpha v$ and the more general form of the critical velocity is

$$v_c = \frac{\Delta}{1+\alpha} \tag{3.45}$$

Lambert predicted that the force and velocity in the pair breaking regime should scale with pressure P as

$$F_{SC} = F\frac{\Delta(P)p_F^3(P)}{\Delta(0)p_F^3(0)} \tag{3.46}$$

$$v_{SC} = v\frac{v_L(P)}{v_L(0)} \tag{3.47}$$

These relationships correctly describe the pair-breaking force measured by tuning forks and vibrating wires [6]. The repeated velocity reversals due to the nature of the vibrating motion lead to the emission of a beam of quasiparticles in the direction of motion [53].

Vibrating objects will also begin to nucleate turbulence at velocities similar to that for pair-breaking. This was first shown to be the case by Fisher [3] via the Andreev reflection of quasiparticles. It is unclear what the exact mechanism for the nucleation of vortex lines is, though turbulence on a vibrating wire can appear in a series of steps, believed to be due to the stretching of remnant vortices [4, 29]. The vortices are believed to develop into a random tangle by the reconnection mechanism described earlier.

3.9 Thermometry Using Vibrating Objects

The damping on vibrating objects at low velocity can be used to calculate the temperature. We can use equation 3.41 and define a constant A such that

$$\Delta f_2 = A \exp\left(\frac{-\Delta}{k_B T}\right) \tag{3.48}$$

this equation can be rearranged to give the temperature T

$$T = \frac{-\Delta}{k_B \ln(\Delta f_2 / A)} \tag{3.49}$$

Using the value of $\gamma' = 0.28$ for a semi-circular vibrating wire [56] we can calculate the constant $A = 1.69 \times 10^5$ for a vibrating wire of diameter 4.5 μm.

To check that the above relation holds, we measure the widths of all of the devices simultaneously as the cell slowly warms after a demagnetisation. We then can then plot each device against the others. This gives us valuable information about various properties of the devices, for example if one device reaches it's intrinsic damping limit while the other is still sensitive to thermal quasiparticles, deviation from the straight line will appear. Subtracting an appropriate value will restore the linearity, and allows us to determine the intrinsic widths. Also, if we have a device for which γ' is known very well, such as a vibrating wire, we can use the ratio of the widths to determine a value of γ' for the other device.

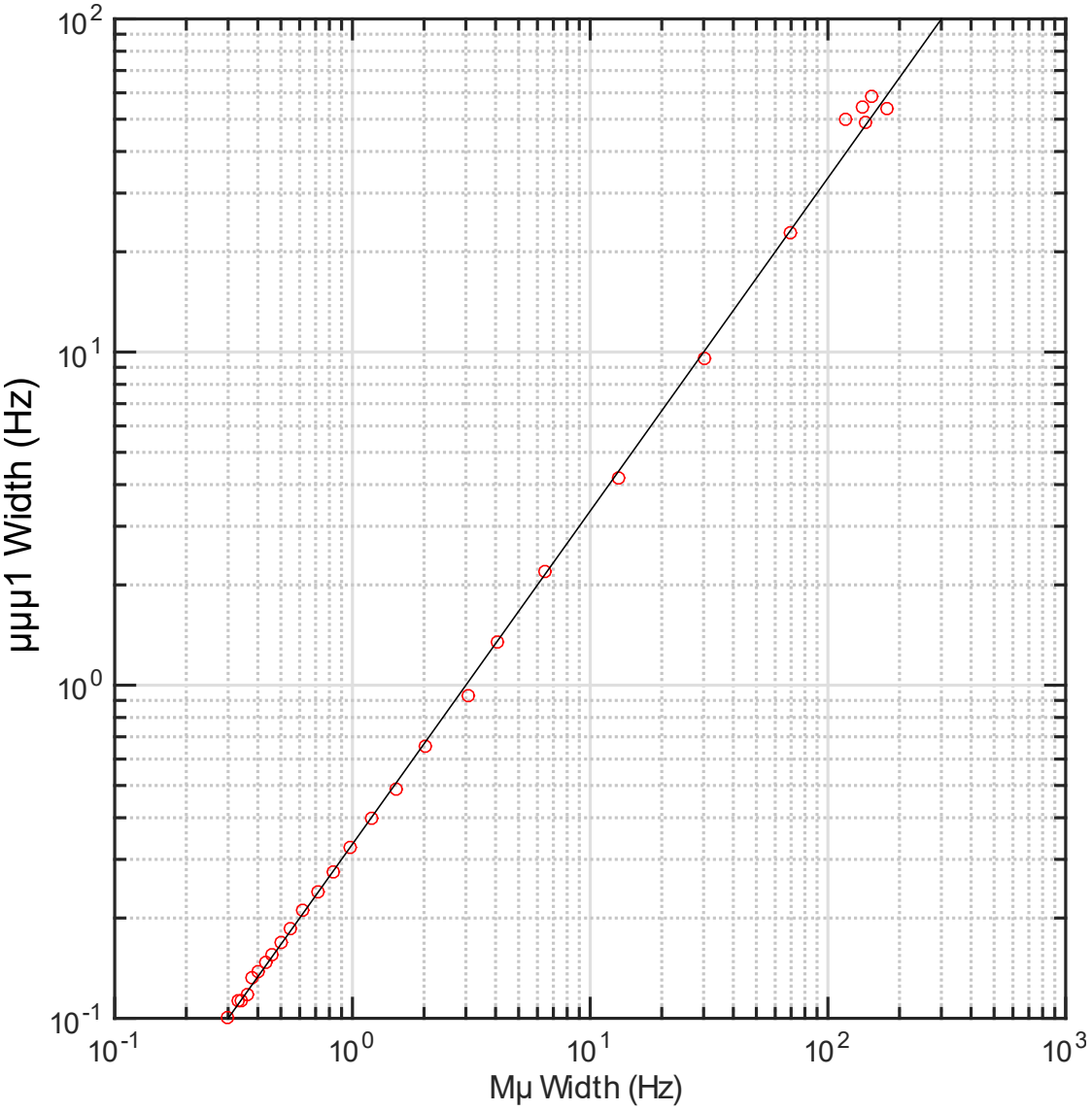

FIGURE 3.12: Width of Mμ against width of $\mu\mu\mu$1 plotted as the cell warms slowly following a demagnetisation

The linear dependence of figure 3.12 shows that the scattering of thermal quasiparticles is the dominant mechanism of damping for both wires. The Mμ wire remains sensitive to thermal quasiparticles to lower temperatures than any other device in the cell. This extra sensitivity is such that we can determine the intrinsic widths of all other vibrating wires and tuning forks by plotting them against the Mμ and

treating the intrinsic width of the device in question as a fitting parameter, which we vary until linearised. We assume when doing this that the intrinsic width of the Mμ wire is still so small compared to the measured width that it may be treated as zero. We have so far been unable to get the experimental cell cold enough to get the Mμ wire to it's intrinsic limit.

A linear fit of the data in figure 3.12 gives a slope of almost exactly 3, which is the ratio of the diameters of the two wires. This confirms that the constant A can be scaled using ratio of the diameters for any semi-circular vibrating wires and we take $A = 5.07 \times 10^5$ as the value for the Mμ wire. It is however, less clear how A will scale between wires and tuning forks, and scaling that has worked previously [6], albeit for a larger tuning fork, does not hold for the ones used here. For any situation where we require the temperature as measured by the tuning forks, we scale the value of A for the Mμ wire by the ratio of the widths of the wire and the tuning forks. We find that the conversion factor between the widths of the tuning forks and the Mμ wire is ~ 0.044.

Chapter 4

Beam Profiles

We visualise turbulence by illuminating the face of the detector with a beam from the BBR, while generating a tangle using the source wire. To analyse how turbulence is produced and distributed we need to know the profiles of the quasiparticle beams from the BBR and the auxiliary beam accompanying the generation of the turbulent tangle by the source wire. In this chapter we describe the calibration of the BBR and how the pixels of our detector are modelled.

4.1 Black Body Radiator Design and Operation

The black-body radiator(BBR) in the experimental cell (figure 3.1) comprises a cubic radiator cavity made from stycast-impregnated paper of side length 5 mm. The walls of the BBR cavity are approximately 0.2 mm thick. The radiator orifice

is formed by drilling a 1 mm diameter hole in the wall, with a stycast-impregnated tracing paper patch glued over the top with a thickness of approximately 0.1 mm. A 0.3 mm hole was then drilled into the patch to form the actual radiator orifice. The smaller the thickness of the wall around the hole, the smaller the reduction in the effective area of the hole due to scattering at the edges of the hole. Furthermore, the edges of the hole are cauterised using a hot needle, to reduce the surface roughness, and to remove any imperfections from the drilling.

The radiator cavity contains two NbTi vibrating wires, constructed as described above. Both vibrating wires have a leg spacing of $D = 3$ mm. One wire has diameter 4.5 μm, and is used as a thermometer and the other has diameter 13.5 μm, and is used as a heater. The direction of motion of the vibrating wire is parallel to the wall with the radiator orifice. Above the pair-breaking critical velocity, the heater wire emits thermal quasiparticles, which traverse the box a number of times and thermalise [9], before being emitted from the orifice in a beam.

4.1.1 BBR Calibration

Calibration of the BBR is performed by measuring the change of the temperature inside as the power applied to the heater wire is increased. The total power entering the black body radiator must balance with the outgoing power emitted from the box orifice. When some power $\dot{Q}_{ap}$ is applied to the heater wire the balance of the incoming and outgoing power is $\dot{Q}_{ap} + \dot{Q}_{hl} = \dot{Q}_{OUT}$ where $\dot{Q}_{hl}$ is the sum of all heat leaks, for example from the walls of the box. Assuming that the gas of excitations

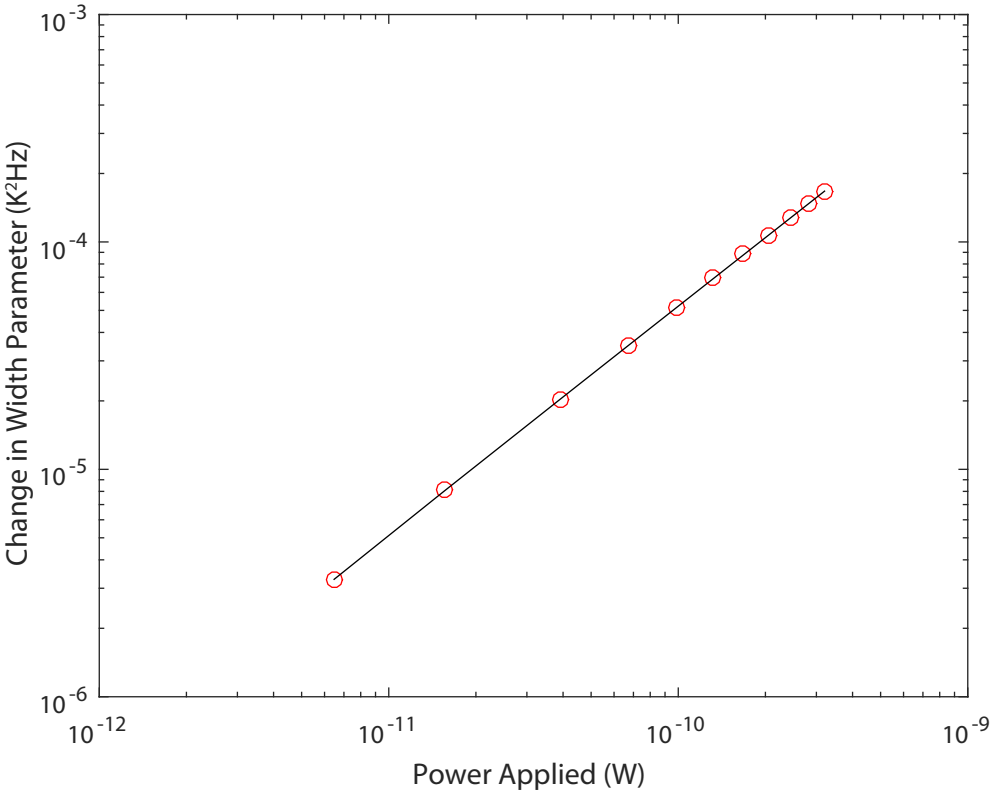

FIGURE 4.1: The calibration plot for the BBR, measured by applying heat using $\mu 2$ and measuring the temperature inside the BBR using $\mu\mu\mu 2$

inside the box is at thermal equilibrium the power emitted from the box orifice is

$$\dot{Q}_{OUT} = \frac{1}{4}\langle n v_g \rangle \langle E \rangle A_h \tag{4.1}$$

where A_h is the effective area of the radiator orifice, and $\langle E \rangle$ is the average thermal energy of quasiparticles, given by

$$\langle E \rangle = \frac{\langle n v_g E \rangle}{\langle n v_g \rangle} = \Delta + k_B T \tag{4.2}$$

Rearranging equations 3.41 and 4.1 yields the following relation for the frequency width and the total power entering the box

$$\Delta f_2 T\langle E\rangle = \gamma' \frac{2dp_F^2}{\pi m k_B A_h} \dot{Q}_{OUT} \tag{4.3}$$

We define the quantity $\Delta f_2 T\langle E\rangle$ as the width parameter. Figure 4.1 is a plot of the change of the width parameter as a function of the applied power $\dot{Q}_{ap}$. Plotting the change in width parameter permits us to estimate the ambient heat leak $\dot{Q}_{hl}$. The slope of the graph can be used to find the value of the constant γ' [56], however in this case we use the simpler relation $W = c\dot{Q}_{ap}$, where c is a constant, to characterise the black-body radiator.

For the BBR used in this experiment we find that $c = 5.22\times10^5$ HzK^2/W. With a value for c, a measurement of the temperature inside the box allows us to use it as a bolometer.

4.1.2 Modelling the Pixels

We treat each of the pixels as cylindrical black-body radiators with both ends open. This assumption describes well the behaviour of the tuning forks inside the pixels. We model the pixel as a cylinder of cross section A_p with both ends open. The total area for the emission of quasiparticles is then $A' = cA_p$ where $c \approx 2$. We assume that the reduction in the effective area of the BBR orifice is small compared to the size of the orifice in this case. For a 'conventional' black-body

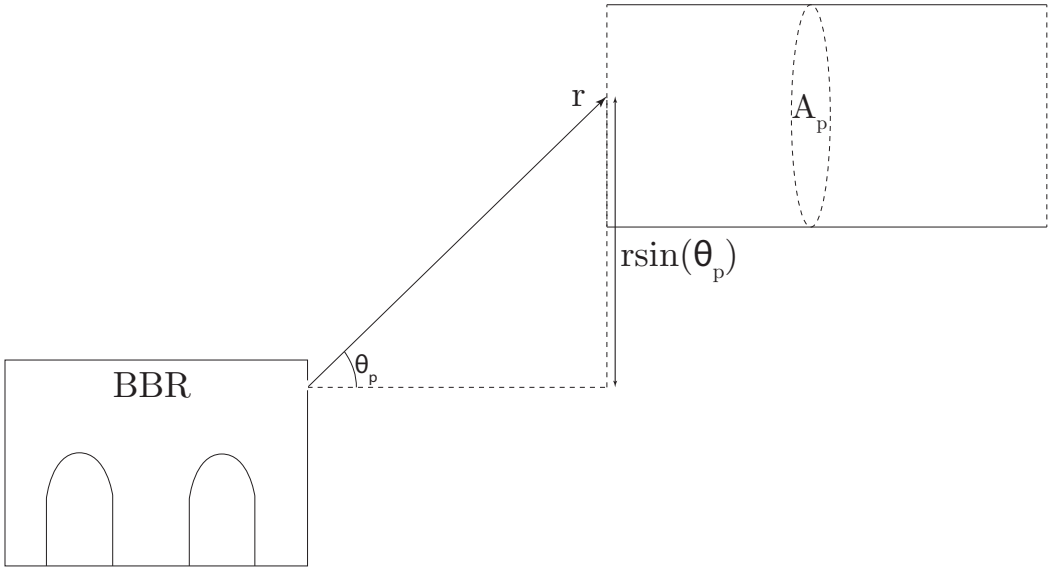

FIGURE 4.2: Diagram(not to scale) showing the construction of the pixel model for a single pixel

radiator with the orifice acting as a point source, the outgoing quasiparticle flux at angle θ and radius r, is

$$\langle nv_g \rangle(\theta, r) = \frac{\dot{Q}}{\langle E \rangle} \frac{cos\theta}{\pi r^2} \tag{4.4}$$

so the power incident on pixel p at distance r_p and angle θ_p is

$$\dot{Q_P} = \frac{A_p \cos^2 \theta_p}{\pi r_p^2} \dot{Q} \tag{4.5}$$

For any BBR, the incoming power must balance with the outgoing power. The incoming power into the pixel is comprised of two main components, the power incident on the pixel from the BBR, and the ambient heat leak from other sources. This ambient heat leak includes a heat leak due to the thermal background in the

cell, which can be characterised by a remote thermometer wire,and a heat leak from the tuning fork itself, due to the electrical connection to the fork in the cell. We label this additional heat leak $\dot{Q_{hl}}$. The balance of all heat leaks into and out of the pixel is then

$$\dot{Q}_{OUT} = \dot{Q}_p + \dot{Q}_{hl} \tag{4.6}$$

The outgoing power can be written $\dot{Q}_{OUT} = \frac{1}{4}A'\langle nv_g\rangle_p\langle E_P\rangle$ and similarly the power due to the heat leak can be written $\dot{Q}_{hl} = \frac{1}{4}A'\langle nv_g\rangle_{hl}\langle E_{hl}\rangle$, hence the balance of power now becomes

$$\frac{1}{4}A'\langle nv_g\rangle_p\langle E_p\rangle = \frac{A_p\cos^2\theta_p}{\pi r_p^2} + \frac{1}{4}A'\langle nv_g\rangle_{hl}\langle E_{hl}\rangle \tag{4.7}$$

The thermal damping can be written ${\Delta f_2}^T = \frac{d\gamma' p_F^2}{\pi m_l k_B T}\frac{\langle nv_g\rangle}{2}$, hence the flux $\langle nv_g\rangle \propto \frac{\Delta f_2 T m_l}{d\gamma'}$. Using this definition, the width parameter in the pixel can be written

$$(W^P - W^{hl}) = W^B\frac{1}{c}\frac{A_h\cos^2\theta_p}{4r_p^2}\frac{d}{T}\frac{\rho_w}{\rho_q}\frac{\gamma'_{TF}}{\gamma'_w} \tag{4.8}$$

Therefore, when analysing the response of the tuning forks, it is possible to calculate the total width parameter in the pixel and then directly subtract the width parameter due to the sum of all heat leaks to recover the width parameter due to quasiparticles originating in the BBR beam.

4.1.3 The Beam Damping

The measured damping on a vibrating object can be broken down into a number of constituent components. There is the intrinsic mechanical damping, that is always present, and we take as the smallest measured damping at the lowest measured temperatures. The remaining damping is due to the quasiparticles interacting with the vibrating object: the damping due to background thermal quasiparticles and the damping caused by the quasiparticles originating from the beam. We can therefore define the beam damping as

$$\Delta f_2^{BEAM} = \Delta f_2^{tot} - \Delta f_2^{Th} - \Delta f_2^0 \tag{4.9}$$

where Δf_2^{tot} is the total measured damping, Δf_2^{Th} is the damping due to thermal quasiparticles, Δf_2^0 is the intrinsic damping. The thermal damping, Δf_2^{Th} for a tuning fork is inferred by converting the damping on a remote thermometer into an effective tuning fork width, based on the thermometry conversion described in section 3.7.

It is also convenient to define the beam width parameter as the width parameter measured by the tuning forks due only to quasiparticles in the BBR beam:

$$W^{BEAM} = W^{tot} - W^{Th} \tag{4.10}$$

where W^{tot} is the total width parameter in the pixel, and W^{Th} is the sum of all

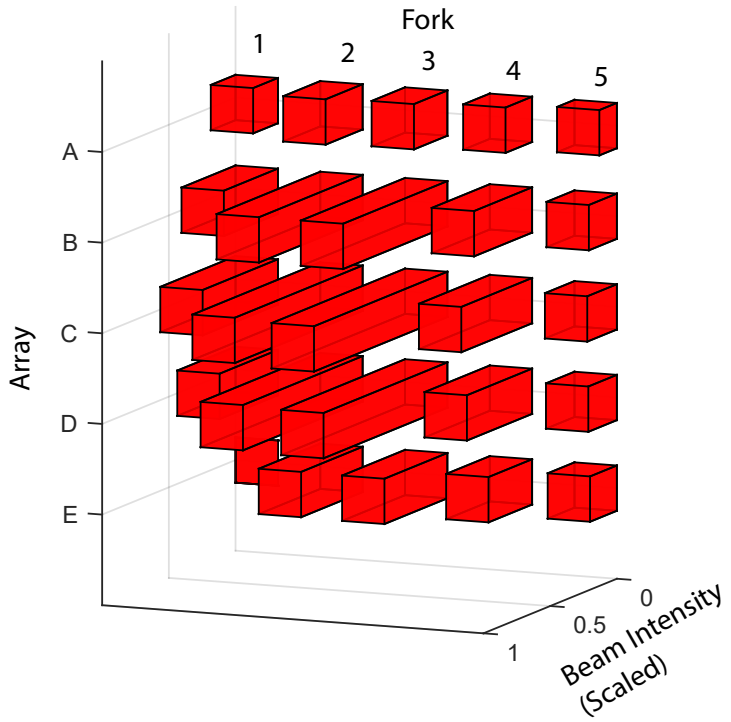

FIGURE 4.3: The profile of the BBR beam, with an applied power of 400 pW

background contributions, including the intrinsic width, the thermal background and other other corrections, such as for a source wire beam, if present.

4.2 BBR Beam Profile

The profile of the beam from the BBR is measured by increasing the power applied to the heater wire, while simultaneously monitoring the damping on all of the tuning forks, the BBR thermometer and a thermometer in the bulk of the cell. Figure 4.3 shows the profile of the beam from the BBR across the detector at a beam power of $\sim$ 400 pW. The damping on each pixel has been normalised by the greatest value(on pixel C3). It is clear from this that the detector is of a sufficient

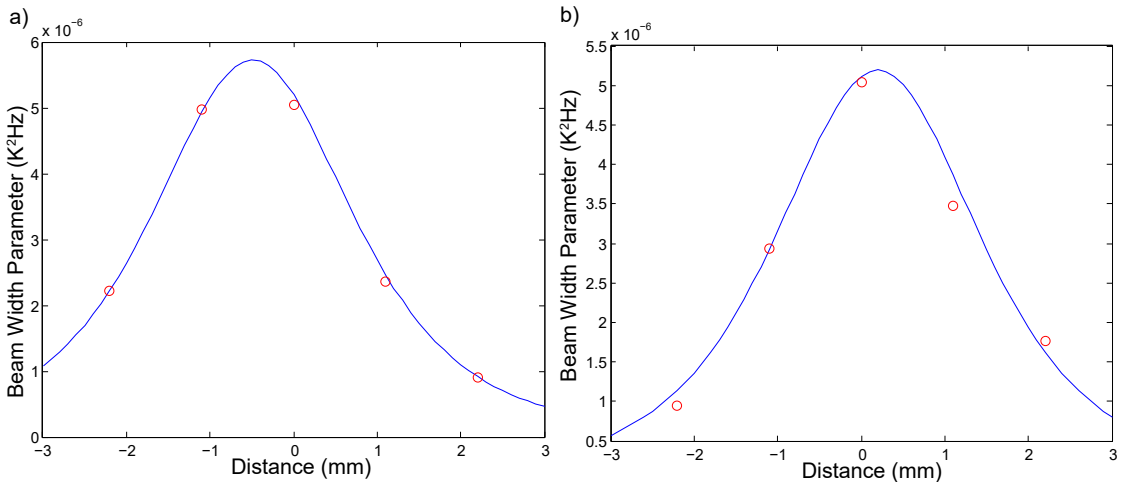

FIGURE 4.4: The profile of the BBR beam across a) the C array and b) the central pixel from each array

size and close enough to the radiator that the beam can be well resolved outside of the noise on each tuning fork, which means that we can use the model described earlier to fit the beam profile along the tuning fork arrays.

Figure 4.4a) shows the horizontal profile plotted along the five pixels that comprise the C array. The solid line on the plot is a fit using equation 4.8. We scale the width parameter measured by pixels C2 and C3 by 20% to account for quasiparticles that pass straight through the detector, based on the geometrical arguments in [37]. This fitting shows that there is a horizontal offset of approximately 0.48 mm. In figure 4.4b) we plot the vertical profile of the central pixel from each array. We fit this profile in the same way and obtain a vertical offset of -0.20 mm. This indicates that a point source is a good model for the orifice of the BBR.

Figure 4.5 shows how the width parameter in the central pixel from each array changes with the power applied to the BBR heater wire. Interestingly, and similarly to the temperature inside the BBR itself, this is a straight line on a logarithmic

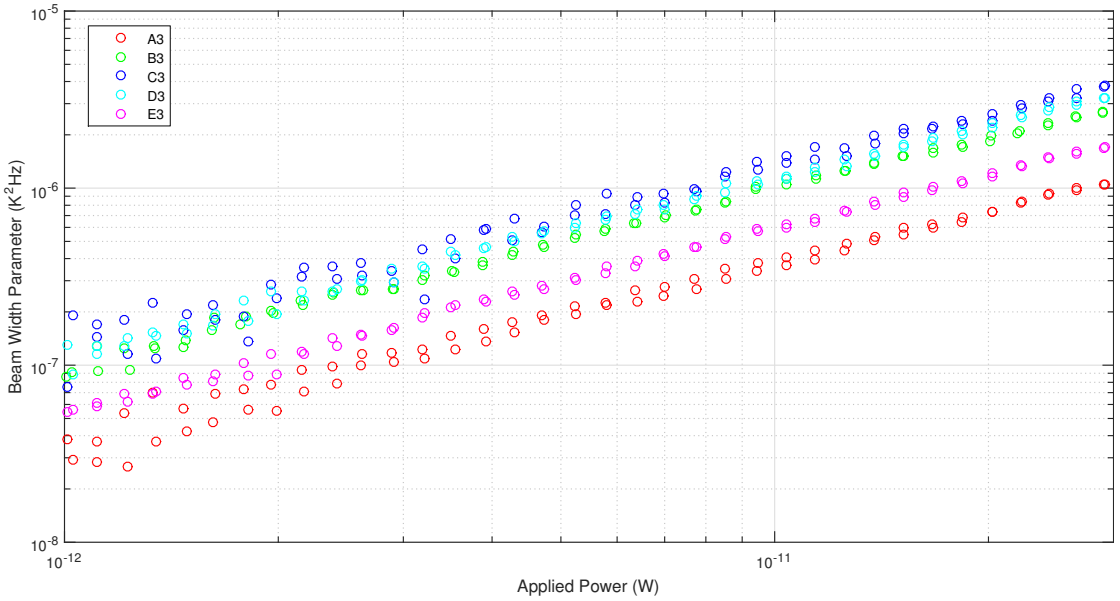

FIGURE 4.5: Plot of the beam width parameter in a selection of pixels as a function of the power applied to the BBR heater wire

scale with a slope of unity.

The fact that the lines in figure 4.5 are parallel indicates that the angular spread of the beam does not change with increasing power. This is consistent with the rapid thermalisation inside the BBR. If the box orifice can indeed be modelled as a point source of excitations, then in principle the power entering each pixel can be calculated. This implies that the detector could be calibrated for use as a array of bolometers and validates the BBR beam as a good illumination source for studies of turbulence.

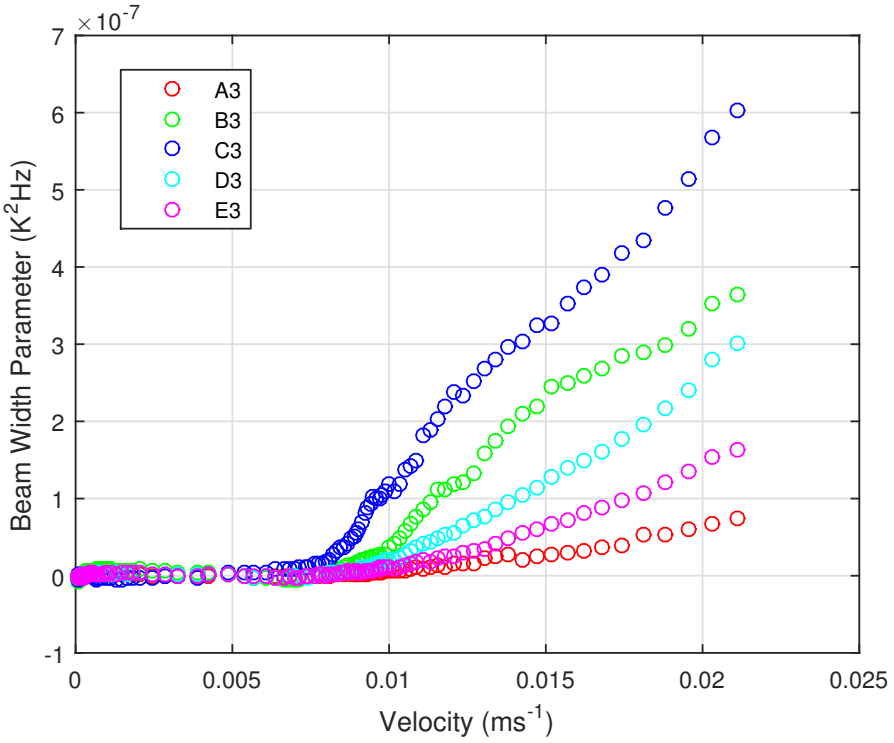

FIGURE 4.6: The beam width parameter in a selection of pixels as a function of the velocity of the source wire

4.3 Source Wire Beam Profile

As mentioned in chapter 3, a vibrating wire, when driven above a critical velocity v_c, will emit a narrow beam of quasiparticles from it's apex. We measure the profile of such a beam by drive-sweeping the source wire from $v \sim 1$ mms^{-1} up to $v \sim 22$ mms^{-1}, with no power applied to the BBR.

In figure 4.6 we plot the beam width parameter in the central pixels as a function of the velocity of the source wire. The beam appears first on the central array, before spreading in the vertical direction as the velocity increases. This is markedly different from the BBR beam, which exhibits no change in angular spread. As the wire reaches the critical velocity, pair-breaking will initially only occur near the

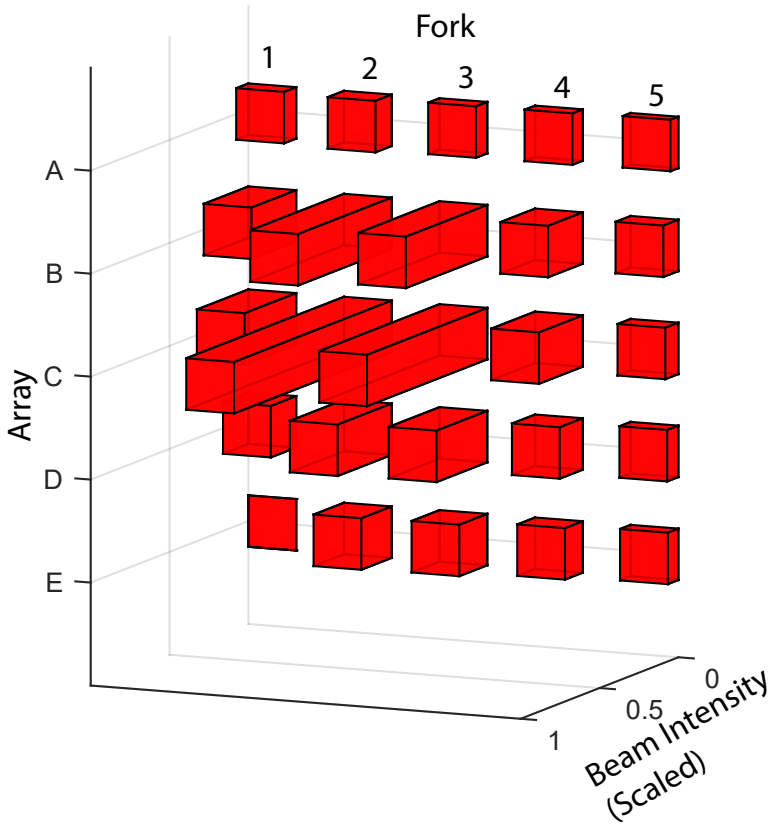

FIGURE 4.7: The profile of the source wire beam at a source wire velocity of $\sim 2.5v_c$

top and bottom of the wire, where the flow velocity is greatest. As the velocity increases, more of the surface area of the wire will contribute to the pair-breaking and the angular spread of the beam will increase [9].

Figure 4.7 shows the profile of the source wire beam across the entire detector at $v \sim 2.5v_c$. It is normalised by the maximum value. It is clear that, when compared to the BBR beam(figure 4.3) that the beam from the source wire is much narrower, particularly in the vertical direction, this is consistent with a beam emitted from a wire loop with an apex in line with the C array.

Figure 4.8a) shows the horizontal profile across the C array. It is clear that the apex of the wire is offset towards pixel 2, and this offset is greater than that of the

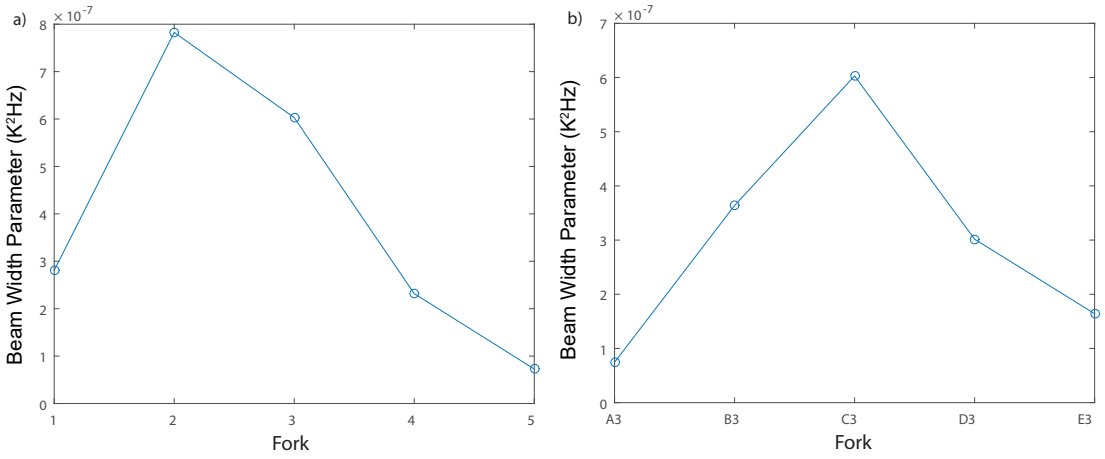

FIGURE 4.8: The profile of the source wire beam across a) the C array and b) the central pixel from each array

box orifice. In figure 4.8b) we plot the vertical profile on the central pixel from each array. It is unclear from this whether there is an offset from the central array in this case. We also observe that the magnitude of the beam from the source wire is approximately an order of magnitude smaller than the beam from the BBR.

In addition, measurements of the shadow cast by a turbulent tangle require that the source wire be driven at a high velocity. At high velocity the magnitude of the shadow is similar to that of the beam, hence the beam profile must be subtracted. It is clear that there is no simple functional form that will fit the beam damping as a function of the velocity, so this subtraction is achieved by linear interpolation.

Chapter 5

Quasiparticle Shadows

In this chapter we will discuss measurements of the quasiparticle shadow cast by a vortex tangle, when it is illuminated by a quasiparticle beam from a black-body radiator. First, we will discuss the reflection of quasiparticles from a vortex flow field, and then we will explain in detail how our measurement data was analysed.

5.1 Andreev-Reflection of Quasiparticles from Vortices

An excitation that passes sufficiently close to a vortex line will be retro-reflected in a process known as Andreev reflection. Andreev reflection passively probes turbulent tangles and permits estimation of the density of the vortex lines in the tangle, provided the approximate extent of the tangle is known.

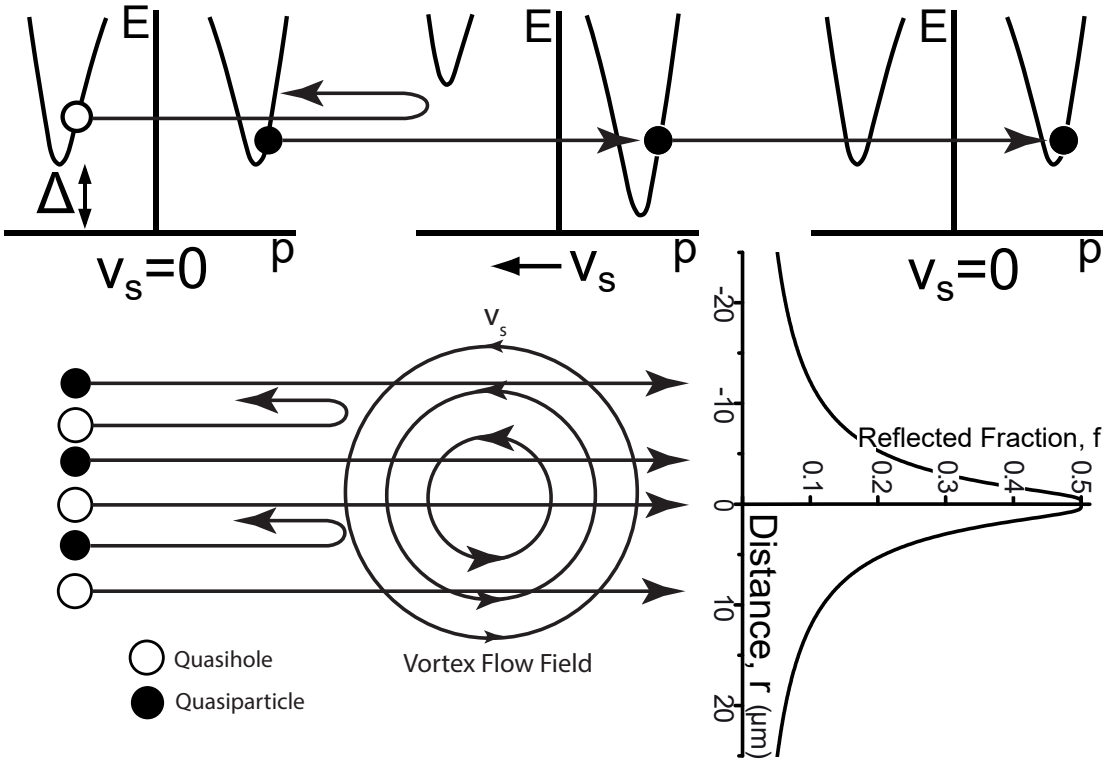

FIGURE 5.1: Interaction of incident quasiparticles with the superfluid flow field around a vortex. The plots at the top show the dispersion curves due to the flow field at the top of the vortex.

The interaction of quasiparticles with the flow field near a vortex line is shown in figure 5.1. The dispersion curves shown are those for the flow field of the top half of the vortex. The flow around the vortex core tilts the dispersion curve, resulting in reflection of a fraction of incident excitations. Flow anti-parallel to the direction of motion reflects quasi-holes and flow parallel to the direction of motion reflects quasiparticles. The higher the energy of the excitation, the closer it must get to the vortex core before being reflected. Recall from chapter 3 that

the flux of quasiparticles incident on the vortex is

$$\langle nv_g \rangle_i = g(E_F) v_F k_B T \exp\left(\frac{-\Delta}{k_B T}\right) \tag{5.1}$$

We first consider the top half of the vortex. The superflow velocity at distance r from the vortex core is $v_s = \hbar/2m_3 r$. Quasiparticles incident on the top half of the vortex can propagate through the flow and are all transmitted. Quasiholes in this region, however, will be Andreev-reflected if they have energy less than $\Delta + p_F \hbar/2m_3 r$. The opposite is true for the flow at the bottom half of the vortex. Hence the flux of excitations transmitted through the flow is

$$\langle nv_g \rangle_t = \frac{1}{2}\left(\langle nv_g + \rangle_i \int_{\Delta + p_F v_s}^{\infty} f(E) g(E) v_g(E) dE\right) \tag{5.2}$$

$$\langle nv_g \rangle_t = \frac{1}{2}\langle nv_g \rangle_i \left[1 + \exp\left(\frac{-p_F \hbar}{2m_3 k_B T r}\right)\right] \tag{5.3}$$

and the fraction of excitations reflected at distance r is

$$f(r) = \frac{(\langle nv_g \rangle_i - \langle nv_g \rangle_t)}{\langle nv_g \rangle_i} = \frac{1}{2}\left[1 - \exp\left(\frac{-p_F \hbar}{2m_3 k_B T r}\right)\right] \tag{5.4}$$

The cross-section for Andreev-scattering is surprisingly large, for example, at 150 μK, $f(r) = 0.1$ at $r = 19$ μm, which is much larger than the vortex core size $a_0 = 60$ nm. A typical quasiparticle excitation with energy $E = \Delta + k_B T$ will be reflected from a vortex line if $\boldsymbol{p}_F \cdot \boldsymbol{v} > k_B T$. This condition is satisfied for

excitations that approach a vortex line within a critical distance

$$r_0 = \frac{p_F \hbar}{2 m_3 k_B T} \tag{5.5}$$

At our lowest accessible temperature, $T \sim 100\ \mu K$, $r_0 = 6.3\ \mu m$ at zero pressure, which is still much larger than the vortex core size. For the reflection from a tangle of quantised vortex lines, we must consider the potential barrier presented by the multiple vortex lines to the transit of quasiparticles.

To estimate the fraction reflected from a tangle of vortices, we model the tangle as a homogeneous slab of vortex lines of thickness Δx and line density per unit area L. Excitations will be Andreev-Reflected if they approach within a distance r_0 of a vortex, hence we model the vortices as tubes of thickness r_0. The probability Δp for an excitation to be reflected is equal to the area that the vortex tubes project onto to the face of the slab, $\Delta p = r_0 L \Delta x$.

We now consider a tangle of thickness d. The probability of an excitation being Andreev-reflected per unit distance is $\Delta p / \Delta x$. The excitation flux in the tangle will decay exponentially with distance, hence to total fraction reflected by a vortex tangle can be written

$$f = 1 - \exp\left(\frac{-d}{\lambda}\right) \tag{5.6}$$

where the decay length is

$$\lambda = \frac{\Delta x}{\Delta p} \approx \frac{2 m_3 k_B T}{\hbar p_F L} \tag{5.7}$$

Re-arranging equations 5.6 and 5.7 allows us to express the line density of the vortex tangle as

$$L \approx -\frac{2m_3 k_B T}{\hbar p_F d} \ln(1-f) \tag{5.8}$$

It should be noted that this is a very rough estimate of the line density as it assumes that the tangle is homogeneous, which is not true in the case of that generated by a vibrating object.

5.2 Experimental Determination of the Reflected Fraction

We can use the model of the pixels to obtain the fraction f of quasiparticles reflected in front of a pixel p in terms of the width parameters inside the pixels and the BBR. We start by assuming that a fraction $(1-f)$ of the total incident power in the direction of p, $\dot{Q}_{Beam}^{Box,p}$ is transmitted through the tangle. Hence the width parameter measured in the pixel in the presence of a tangle can be written

$$W_{beam}^{P} = (1-f) W_{beam}^{Box,p} \tag{5.9}$$

where $W_{beam}^{Box,p}$ is the width parameter due to the quasiparticles emitted from the BBR towards pixel p. This quantity is proportional to the total width parameter in the BBR. In the presence of a turbulent tangle, a fraction of the quasiparticles will be reflected back into the BBR, reducing the beam power. The width parameter

measured in the pixel is then reduced by two effects, the shadow cast by the turbulent tangle, and the reduction in the beam power. To eliminate the effect of the reduction in beam power we scale the measured width parameter by the ratio of the width parameter measured in the BBR with and without turbulence. We can then write the width parameter measured in the pixel due to quasiparticles originating from the BBR and in the presence of turbulence as:

$$W^p_{Beam}(v_s) = (1-f)W^p_{Beam}(v_s=0)\frac{W_{Box}(v_s=0)}{W_{Box}(v_s)} \tag{5.10}$$

where v_s is velocity of the source wire. The fraction of quasiparticles reflected in front of pixel p is

$$f = 1 - \left(\frac{W^P(v_s)}{W^P(v_s=0)}\frac{W_{Box}(v_s=0)}{W_{Box}(v_s)}\right) \tag{5.11}$$

5.3 Quasiparticle Shadows across the Detector

The measurement described here is performed by driving the source wire at some high velocity, typically $v \sim 2.5v_c$, sufficient to generate a fully developed turbulent tangle, while the detector is illuminated by a beam from the black body radiator. To observe the shadow cast by the turbulent tangle we drive the tuning forks non-linearly, to improve the signal-to-noise ratio in the measurement. The power applied to the BBR is chosen such that the mechanical time constant for the measurement of the tuning forks is below 0.1 s and that data can be acquired at a

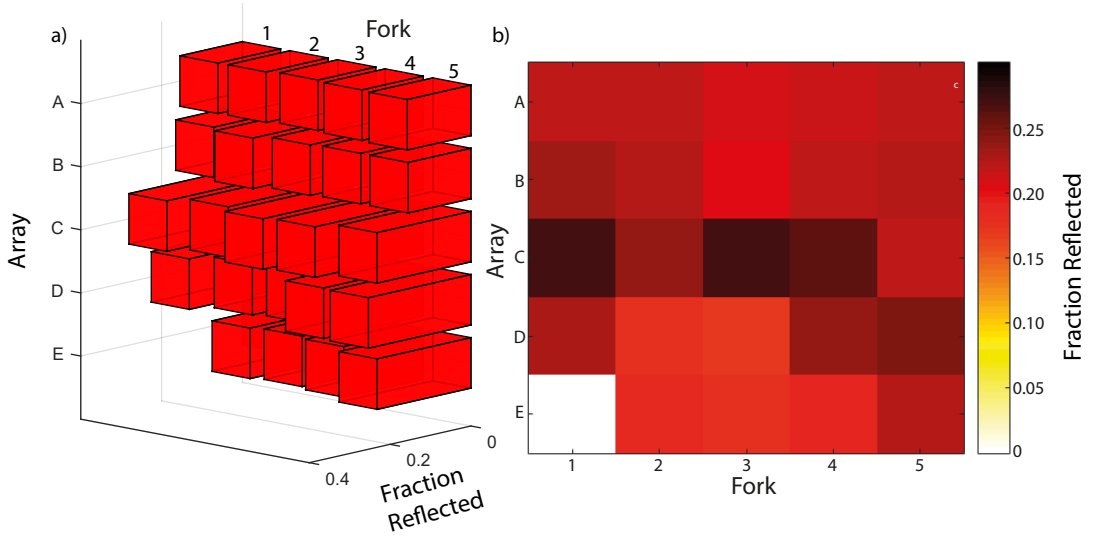

FIGURE 5.2: Profile of the quasiparticle shadow cast by a turbulent tangle at wire velocity $v = 2.5v_c$. Figure a) shows a 3D plot of the shadow, where the length of the bars show the fraction of quasiparticles reflected, b) shows the same profile as a 2D grid, allowing easier visualisation of the profile.

rate of ~ 10 Hz. The beam power required is such that the shadow signal is much larger than the noise of the tuning forks, but the cell does not warm too quickly. Measurements at beam powers greater than 800 pW show that the cell warms to the extent that measurement becomes impossible within an hour.

Large number of pixels covering an area of 25 mm^2 allows us to investigate the spatial variation of the fraction of quasiparticles reflected and reveals how turbulence is distributed around the source wire. Figure 5.2 shows the profile of the shadow cast by a tangle generated at wire velocity $v = 2.5v_c$.

Overall, the Andreev reflection observed is evenly distributed with the exception of the middle row, the 'C' array. In accordance with chapter 4, this array is approximately in line with the apex of the source wire. The apex is the part of the wire

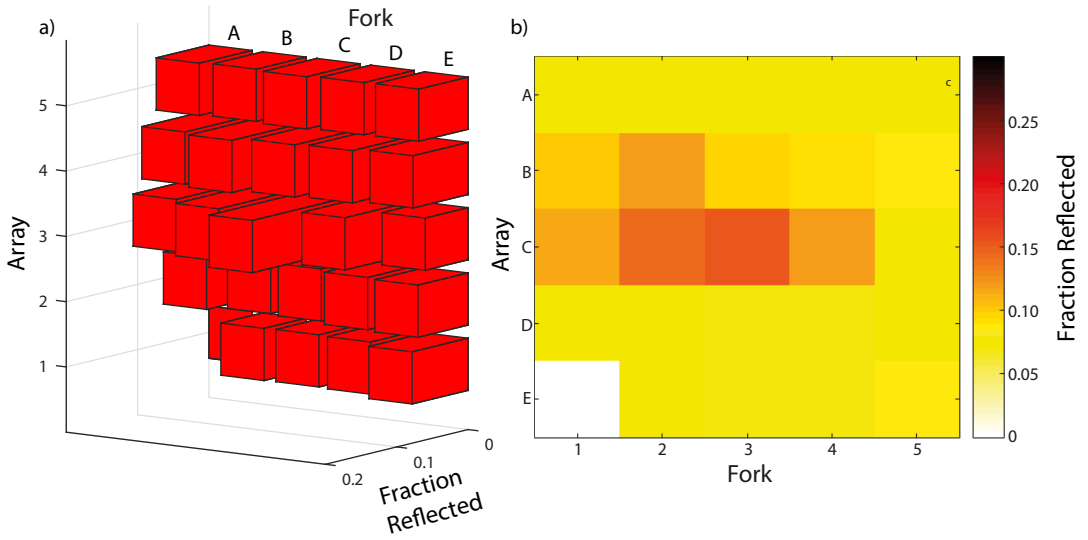

FIGURE 5.3: Profile of the quasiparticle shadow cast by a turbulent tangle at wire velocity $v \approx v_c$. Figure a) shows a 3D plot of the shadow, where the length of the bars show the fraction of quasiparticles reflected, b) shows the same profile as a 2D grid, allowing easier visualisation of the profile.

that moves at the greatest velocity, and hence it is thought that turbulence nucleation will occur first in this region, before spreading further along the wire. Thus we might expect that the vortex line density, or the spatial extent of the tangle is greatest in the region around the surface of the wire due to continuous emission of vortex rings from the active region near the apex of the wire. These vortex rings reconnect as they move away from the wire, resulting in a random tangle further away from the wire. In this case the greatest fraction reflected, measured on the C array, is $f = 0.25$. Using equation 5.8 and assuming that the spatial extent of the turbulence is 2 mm we estimate the line density as $L = 3.4 \times 10^7$ m^{-2}, similar to that calculated for a vibrating grid at high velocity [52].

Figure 5.3 shows the profile of the shadow cast by a tangle generated at source wire velocity $v \approx v_c$. It is clear that, even at velocities close to the critical velocity,

the behaviour is similar to that observed at high velocites, albeit with a smaller reflected fraction.

It is clear from these measurements that the Andreev reflection technique has great potential to investigate properties of the turbulent tangle, though it requires careful optimisation to do so. It would be interesting to consider different geometries for the detector and source wire arrangement, for example using a wire that vibrates in the direction parallel to the face of the detector, or if possible, a simultaneous measurement for both projections. For example, it has been shown that the turbulence will spread from a vibrating wire along the quasiparticle beam path [57], so it would be interesting to investigate whether it would be possible to use two detectors and two projections of the spatial variation of the vortex line density to measure and reconstruct a three dimensional turbulent tangle.

Chapter 6

Turbulent Screening

The measurements described in this chapter are typically performed by drive-sweeping the source wire whilst the detector is illuminated by a beam of quasiparticles from the BBR. We calculate the fraction of quasiparticles reflected in front of each pixel as a function of the velocity of the source wire to investigate the development of the tangle and it's properties.

Figure 6.1a) shows the fraction of beam quasiparticles(eq 5.11) reflected in front of pixel C3 (blue line) and the force-velocity profile of the source wire (red line). The critical velocity of the source wire, determined from figure 3.10, is approximately $v_c = 8$ mms^{-1}. As expected the fraction of quasiparticles reflected is zero below the critical velocity and starts to rise sharply as the critical velocity is reached. The reflected fraction increases until $1.3v_c$, where it reaches a plateau and remains constant until approximately $2.5v_c$, where the reflected fraction starts to rise again,

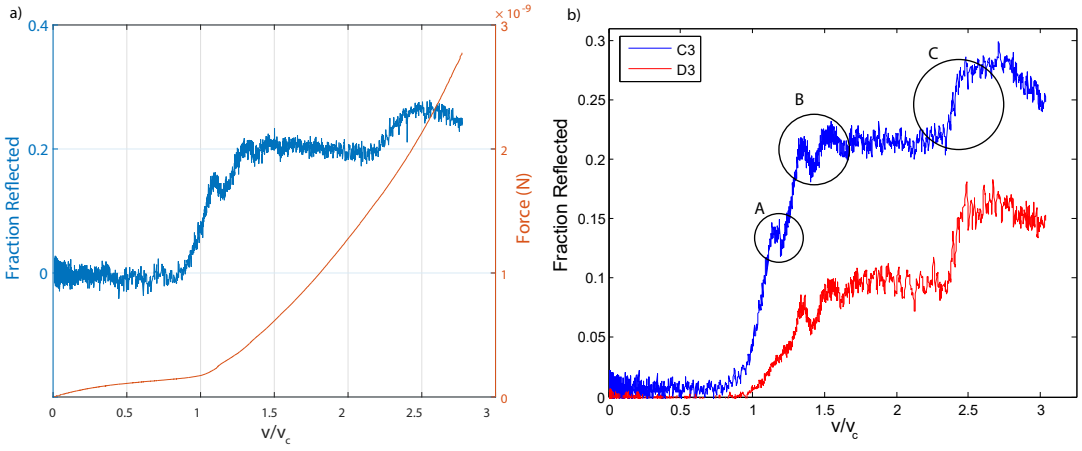

FIGURE 6.1: Plots a) of the force-velocity profile of the source wire(red) and the fraction reflected in front of pixel C3(blue) and b) of the fraction reflected in front of pixels C3 and D3 as a function of the source wire velocity

before plateauing once more. At the very highest velocities the reflected fraction starts to decrease once again, this could be due to the beam from the source wire starting to affect the measurement, as the tuning fork response to the beam has a similar magnitude to the shadow cast in this regime.

Figure 6.1b) shows the fraction reflected as a function of source wire velocity in front of pixels C3 and D3. It is clear that the overall behaviour on both forks is similar. There are three interesting features in figure 6.1b), which are labelled A, B and C. These features are reproducible over a number of measurements and separate experimental runs, indicating that they are properties of the turbulence generated by the source wire.

The features are not accompanied by changes in the slope of the force-velocity curve. A possible explanation is that during increases in the reflected fraction, both a beam and turbulence are produced by the vibrating wire, while during plateaus the vortex production is suppressed. Alternately, it could be that at each

feature the structure of the turbulence is changing, for example, they could indicate points at which vortex rings reconnect into a tangle.

Figure 6.2 shows the fraction of quasiparticles reflected in front of fork C3 for two different types of measurement. The solid line is measured during a drive sweep of the source wire, where the velocity is almost continously changing ($<$ 1s at each point). To ensure that the features A, B and C were not artifacts of the nature of the measurement, the discrete points were measured by choosing a number of values for the velocity. At each point the velocity was maintained for approximately 200 s, a trace of feature A is shown in the inset of figure 6.2. It is clear from the graph that the features A, B and C exist in both measurements, reinforcing the idea that they are a property of the turbulence generated by the wire, and not simply artifacts resulting from the measurement method.

6.1 Shadow as a function of the applied power

Figure 6.3 shows the vortex signal of pixel C3 as a function of source wire velocity for a variety of different BBR beam powers. We define the vortex signal S as:

$$S = fT \tag{6.1}$$

The vortex signal is independent of temperature and allows a direct comparison between different BBR beam powers.

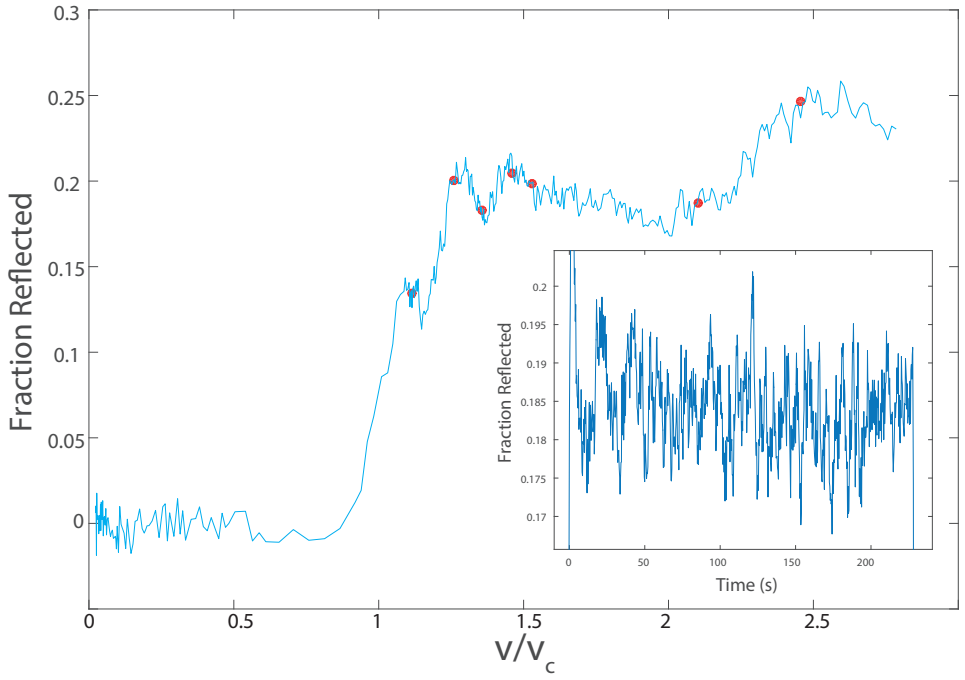

FIGURE 6.2: The fraction of quasiparticles reflected in front of fork C3 for a continuous measurement(solid line) and for discrete points(points) as a function of $\frac{v}{v_c}$

The turbulence generated by the source wire should not depend on the power applied to the BBR. However, it is possible that for very large powers, the quasiparticles emitted by the BBR could interact with vortex cores and push the turbulence away from the wire. In our case, for the central fork C3 it appears that if any effect exists, it is below the limits of our sensitivity, hence can be neglected. This confirms that, within our resolution, beams of the powers described here are passive probes and have no effect on the measurement itself. Extending this analysis to higher powers (greater than $\sim$ 600 pW) presents further problems, however, as these beam powers will cause the cell to warm within an hour, and measurements become impossible.

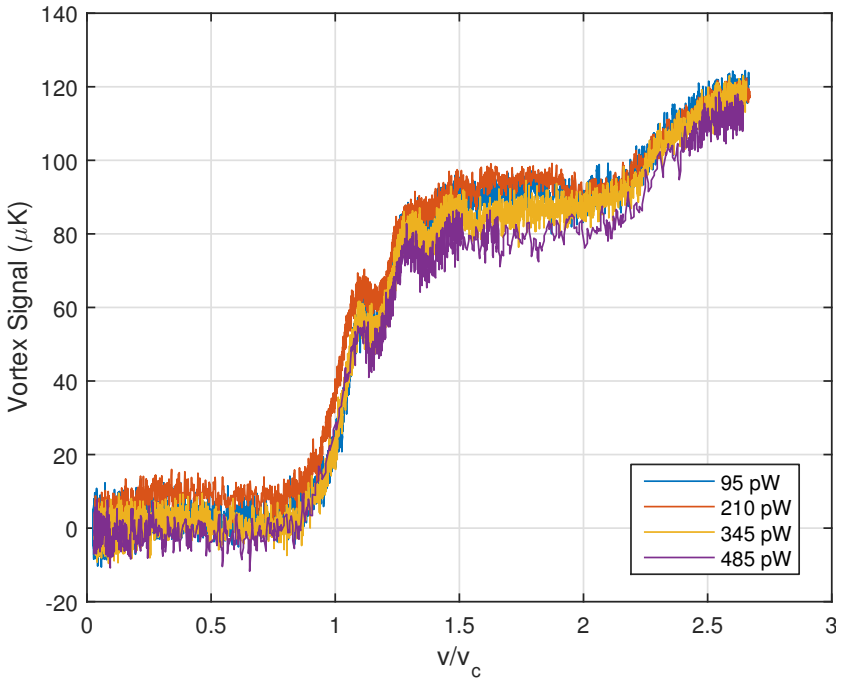

FIGURE 6.3: The vortex signal of C3 as a function of $\frac{v}{v_c}$, for a variety of different BBR beam powers

6.2 The Spread of the Turbulent Tangle

Previously [8], cross-correlation of the vortex signal measured by several detector wires was used to estimate the propagation velocity of a turbulent tangle generated by a grid. In principle, our detector could be used to investigate the propagation velocity perpendicular to the direction of wire motion. Our measurements show that there is no delay in the spread from the central pixel C3 to any of the outer pixels C5, A3 or A5, within the time resolution of the data measured here (~ 0.1 s). This indicates that the turbulent tangle fills the volume illuminated by the beam in less than 0.1 s.

Another way of investigating the spread of the tangle is to consider how the fraction reflected as a function of velocity differs for different pixels. We plot the fraction

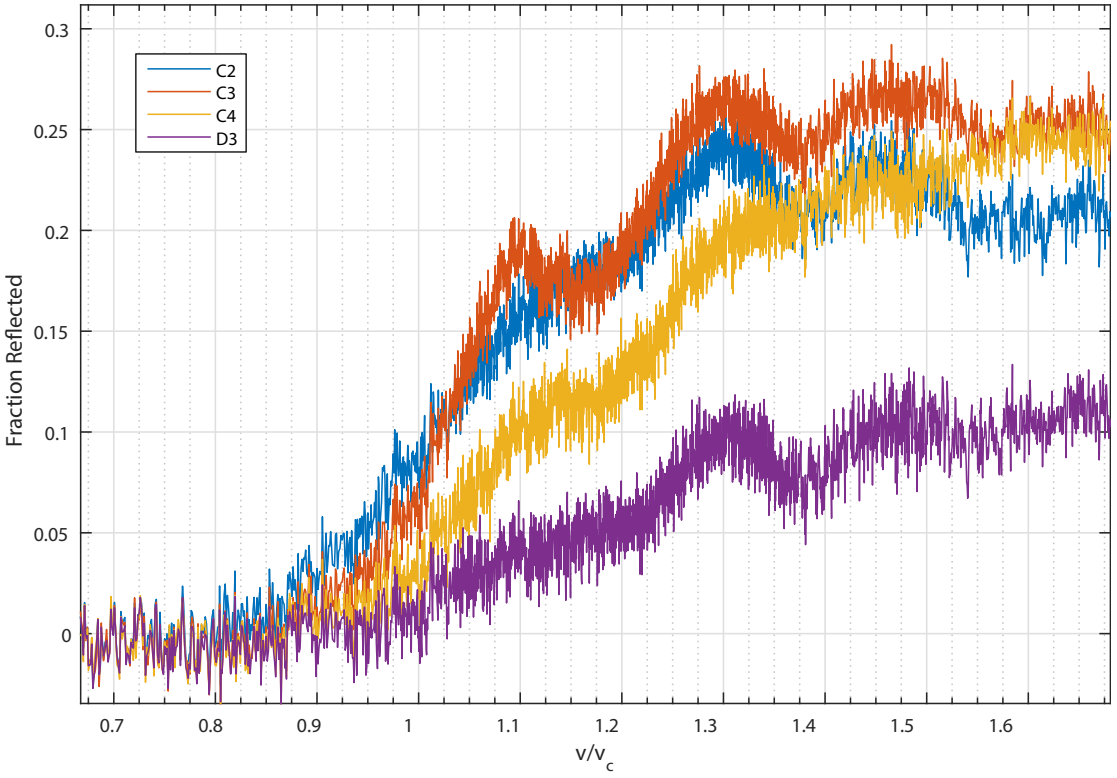

FIGURE 6.4: The fraction of quasiparticles reflected in front of a number of forks as a function of $\frac{v}{v_c}$

reflected as a function of the source wire velocity for forks C3, C2, C4 and D3, in figure 6.4 and can see some differences in the way that the shadow develops. In the case of C3 and C4, the fraction reflected in front of C3 initially rises much faster than that in front of C4, before they both attain the same level. This implies that the vortex line density increases in front of C2 and C3 first, before spreading along the array. In addition to this, at $\sim 1.1v_c$, the feature labelled A earlier exists much more clearly on C3 that the other forks, implying that the details of the vortex line density in front of C3 are in some way different to that in front of the other forks. The remaining features are not consistent across the other forks, hinting at some spatial variation in the development of turbulence, but greater spatial resolution

would be required to comment further.

6.3 Fraction reflected into Box

We can also calculate the fraction of quasiparticles that are reflected into the box directly by measuring the BBR thermometer during pulses and drive-sweeps of the source wire. Recall from chapter 4 that the balance of all heat leaks into the box is

$$\dot{Q}_{OUT} = \dot{Q}_{ap} + \dot{Q}_{hl} + \dot{Q}_{Th} \tag{6.2}$$

when there is a turbulent tangle in the beam path some fraction, f, of the outgoing power will be reflected back into the box. At very high source wire velocities there will also be an appreciable heat leak, $\dot{Q}_s$, into the box from the beam emitted by the source wire. Hence, the balance becomes

$$\dot{Q}_{OUT} = f\dot{Q}_{OUT} + \dot{Q}_{ap} + \dot{Q}_{hl} + \dot{Q}_{Th} + \dot{Q}_s \tag{6.3}$$

which can be rearranged to give the fraction reflected

$$f = 1 - \frac{\dot{Q}_{ap} + \dot{Q}_{hl} + \dot{Q}_{Th} + \dot{Q}_s}{\dot{Q}_{OUT}} \tag{6.4}$$

All of the heat leaks into the box can be determined experimentally, hence we can find the fraction of quasiparticles reflected into the box and compare it to

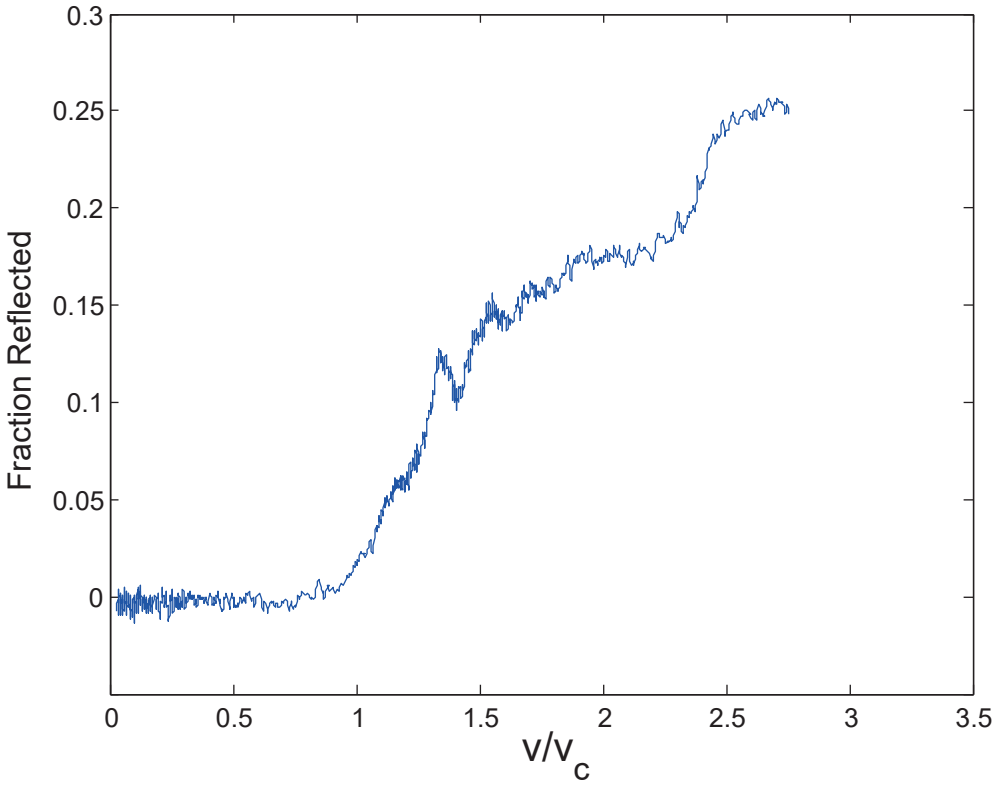

FIGURE 6.5: The fraction of quasiparticles reflected back into the BBR as a function of the source wire velocity

that measured in front of a pixel. Figure 6.5 shows the fraction of quasiparticles reflected back into the BBR as a function of the source wire velocity. It is clear that this is very similar to that measured for pixel C3, including the aforementioned features. This, again, indicates that they are properties of the development of the turbulent tangle.

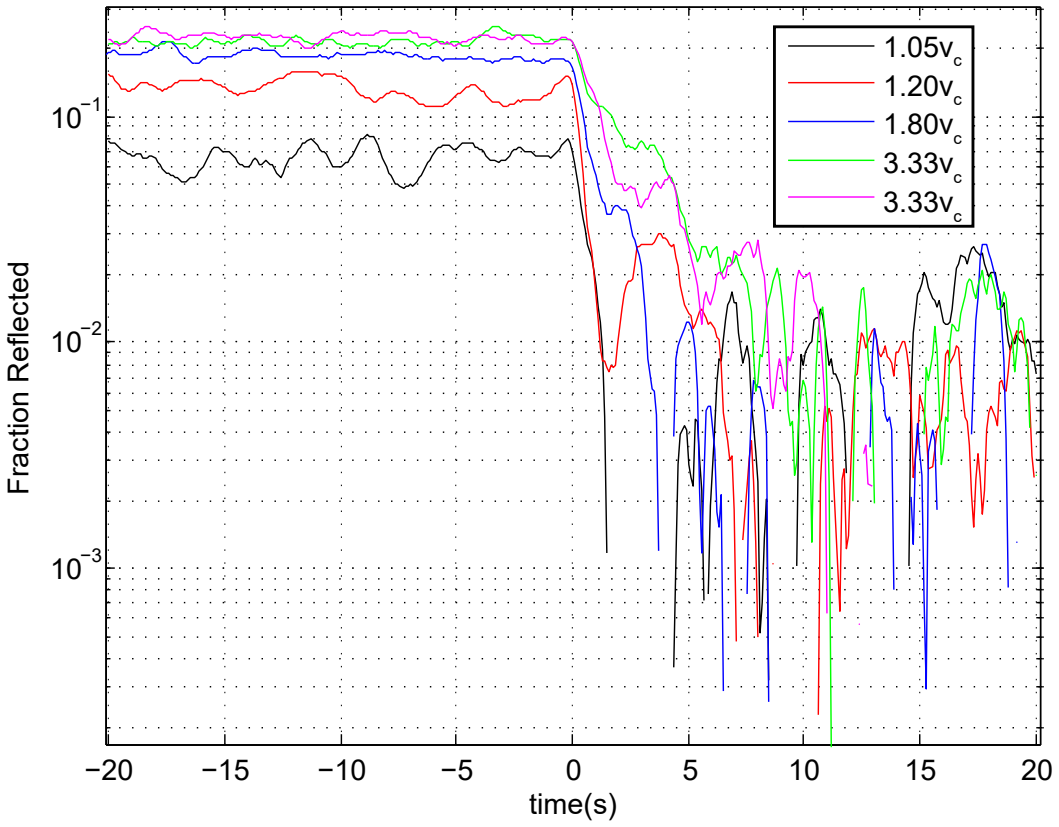

FIGURE 6.6: The decay of the vortex signal as a function of time after turbulence generation is stopped, for a variety of source wire velocities

6.4 Decay of Turbulence

It has been shown [8] that for turbulence generated by a vibrating grid, the decay time of the vortex signal will increase as the driving velocity of the grid is increased. This has been linked to the idea that at lower velocities the turbulence is comprised mainly of vortex rings, which will decay almost instantly after turning the drive to the grid off. At higher velocities it is thought that the vortex rings recombine into a random tangle that shows a $t^{-3/2}$ decay. In the case of the grid it was also observed that the vortex signal would initially decay quickly, followed by the slow

decay, which was postulated to be due to the decay of vortex rings followed by the decay of the tangle. In this case we are investigating the properties of a tangle generated by a more simple vibrating loop, which could have different properties. Figure 6.6 shows the decay of the reflected fraction in front of pixel C3 as a function of the time after the drive to the source wire is switched off. It appears that the decay time does increase as the driving velocity is increased, but the noise in the measurement is such that the signal rapidly descends into noise before a good measurement of the decay powerlaw can be taken. In this case however, it appears that at high velocity there is no fast decay immediately after switching the drive off, possibly indicating that the vortex signal we measure is almost entirely due to the vortex tangle and not due to vortex rings.

Chapter 7

Turbulent Fluctuations

In the presence of a turbulent tangle, the noise in the tuning fork signal increases, as shown in figure 7.1a). We attribute this to fluctuations in the vortex line density in the tangle [58]. These fluctuations can be used to investigate the development of the turbulent tangle, statistical properties of the turbulence, and, in principle, to investigate whether we can observe individual vortex rings and vortex lines within the overall shadow.

7.1 Amplitude of Fluctuations and Development of the turbulent tangle

Figure 7.1b) shows an example of a Gaussian fit to the fluctuation amplitude at source wire velocity $v \sim 2.5 v_c$, where the fluctuations are clearly visible. We find

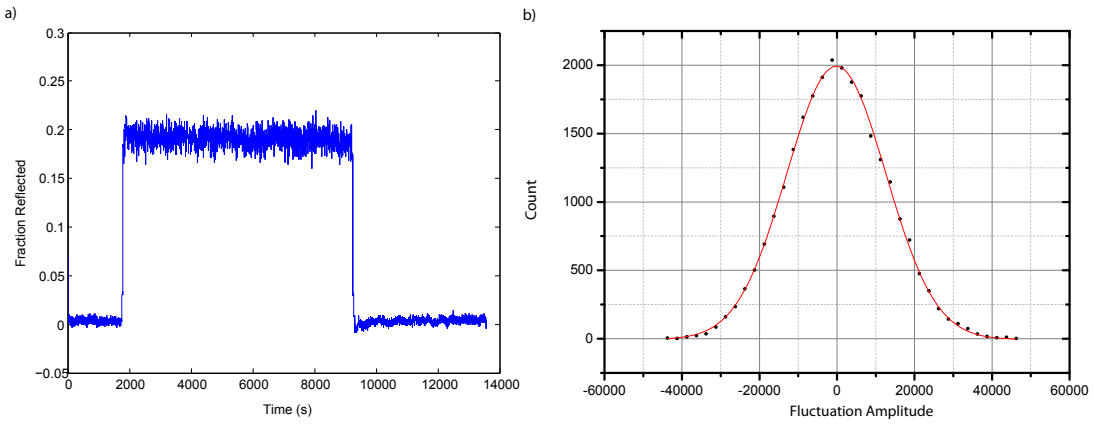

FIGURE 7.1: a) The fraction of quasiparticles reflected in front of fork D3 during a pulse of turbulence and b) Gaussian fit to the fluctuation amplitude at source wire velocity $v = 2.5v_c$, performed by removing the background from a) and binning the data.

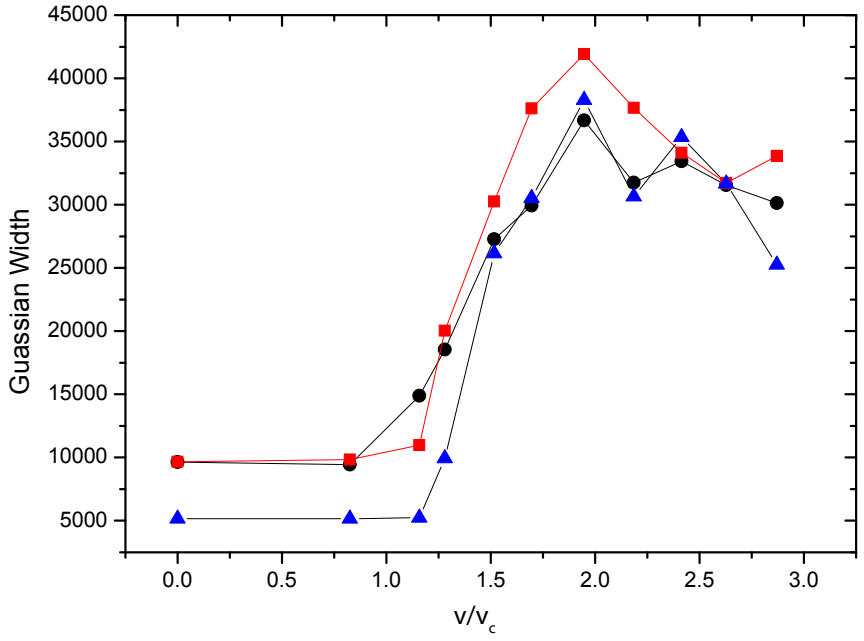

FIGURE 7.2: The width of the Gaussian fit as a function of the velocity of the source wire for pixels C3(black circles), C2(red squares) and D3(blue triangles)

the fluctuation amplitude by removing the background, and then bin the data to from a histogram. The Gaussian distribution provides a very good fit to this data for all source wire velocities. We define the amplitude of the fluctuations as the width at half-height of the Gaussian fit.

It can clearly be seen in figure 7.2 that the fluctuation amplitude remains constant (and is just a measure of the background noise) below the critical velocity. This is obviously to be expected, since there are no vortex lines and hence no line density fluctuations. Above the critical velocity the fluctuation amplitude increases rapidly and attains some a maximum value by the at $v \sim 2v_c$. At very high velocities, approaching the Landau critical velocity (27 mms^{-1} or $\sim 3v_c$), the fluctuation amplitude actually appears to start dropping. This appears similar to the behaviour of the fraction of quasiparticles reflected, which was earlier attributed to the increase in the thermal damping due to the source wire beam. It could be that the source wire beam also has an effect on the fluctuation amplitude, though it is not clear how this could be.

7.2 The Frequency Spectrum of Turbulent Fluctuations

As mentioned previously, at large length scales, quantum turbulence decays consistently with having a Kolmogorov-like spectrum (equation 2.14), which incorporates an $k^{-5/3}$ dependence. We can investigate this in our cell by performing a power fast-Fourier transform(FFT) of the tuning fork signal in the presence of turbulence. It can clearly be seen from figure 7.3 that the spectrum shows an $f^{-5/3}$ powerlaw. This is reminiscent of the behaviour exhibited by Kolmogorov turbulence. We are however limited to frequencies below ~ 1 Hz due to the mechanical time constant

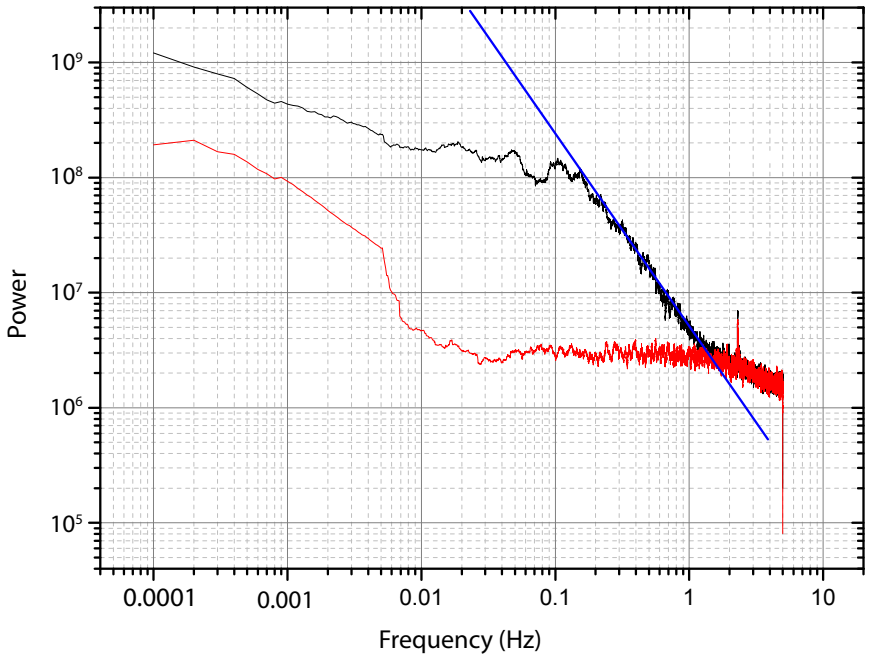

FIGURE 7.3: The frequency spectrum of the noise on tuning fork C3 in the presence of turbulence(black line) and with no turbulence present(red line). The blue line is a guide showing an $f^{-5/3}$ decay.

of the tuning forks, which can be determined from the linewidth of the resonance and we take as $1/\pi\Delta f_2$.

7.3 Single Vortex Structures Within the Shadow

One of the goals of a detector of quasiparticle flux is to be able to capture images of the shadow cast by single vortex structures such as lines and rings. This requires that the detector be sensitive to shadows of this level. The fraction of quasiparticles reflected by a vortex line is given by equation 5.4. We consider a straight vortex line of length L pinned across the face of a cylindrical pixel of diameter $2r_p$, with the centre of the pixel at $r = 0$. On one side of the vortex line quasiparticles will be

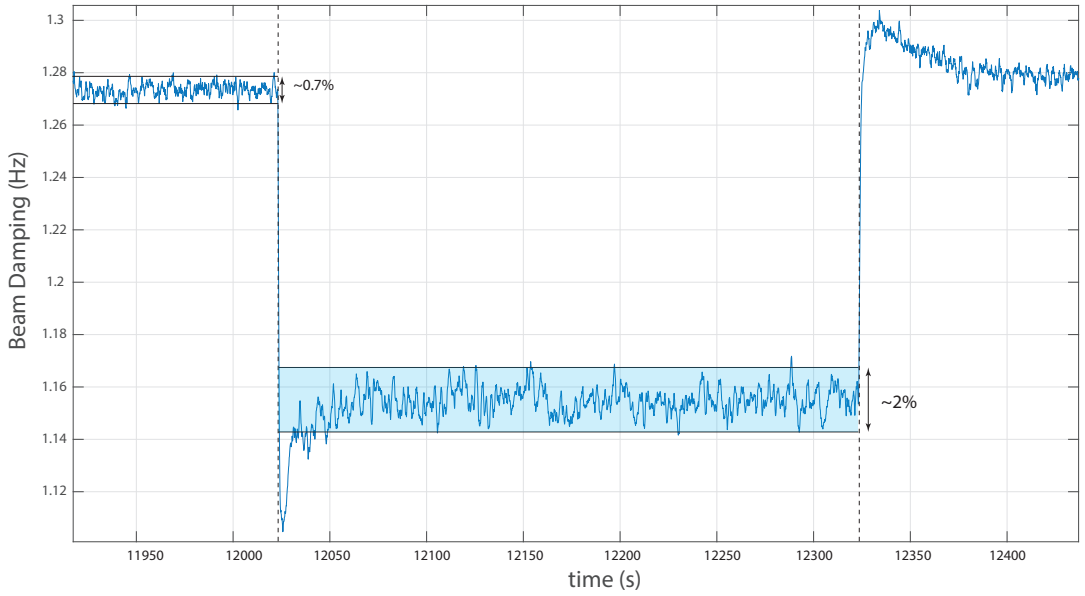

FIGURE 7.4: The vortex signal on a tuning fork as a function of time, showing the sensitivity level required to observe single vortex structures

reflected, and on the other quasiholes, depending on the sense of the circulation. We can calculate the flux of reflected excitations that would otherwise reach the pixel $\dot{N}_R$ by integrating the fraction reflected from the centre of the pixel to r_p on either side of the vortex.

$$\dot{N}_R = \frac{2L}{A}\int_0^{r_p}\frac{1}{2}f(r)dr = \frac{1}{2} - \frac{1}{2r_p}\int_0^{r_p}\frac{1}{2}\exp\left(\frac{p_F\hbar}{2m_3k_BTr}\right)dr \tag{7.1}$$

where A is the area of the pixel. Evaluating this integral for a pixel with $r_p = 0.5$ mm shows that approximately 2% of the quasiparticles would be reflected by a vortex line pinned across the opening of the pixel. If the noise level of the tuning forks is less than this value, it is, in principle, possible to detect a single vortex line.

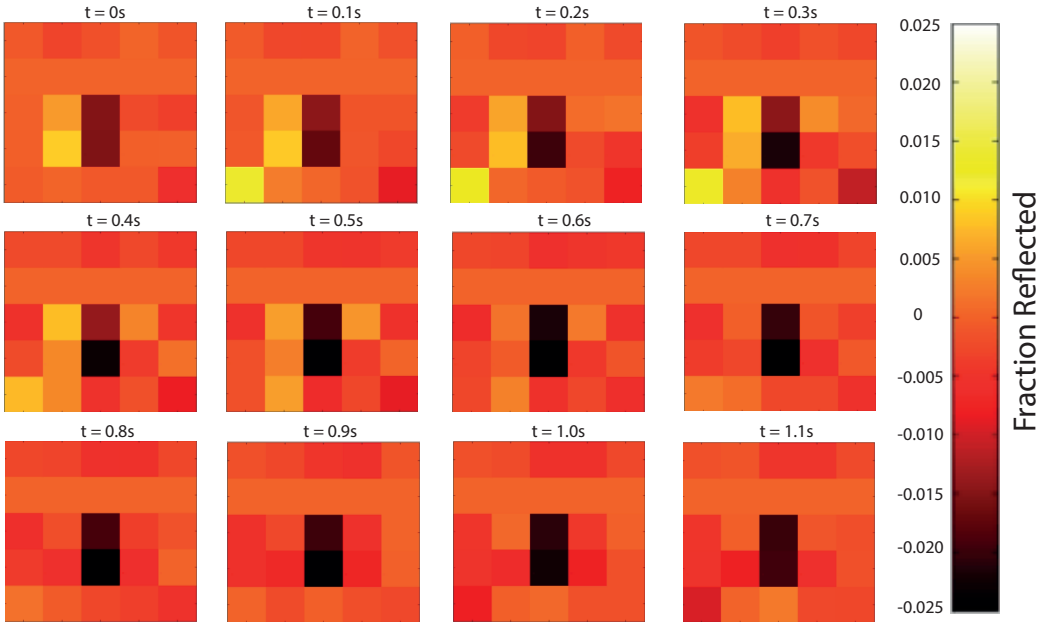

FIGURE 7.5: A sequence of camera images showing an example of a candidate of a vortex line moving across the face of the detector

Figure 7.4 clearly shows that the detector noise level is below the limit for detection of a single vortex line. The next challenge is extracting data that indicates a single vortex line moving across the front of a pixel and representing this event in a meaningful way. One way of representing this data is to consider the shadow cast on the detector as a function of time, and look for events where a number of pixels indicate an increased shadow. Figure 7.5 shows a candidate event for the pinning of a single vortex line across the pixel. The images are plotted such that a black pixel indicates a 2% shadow on a pixel. This sequence clearly shows an event where the shadow cast on C3 and D3 is much greater than the surroundings, possibly indicating a vortex line pinned across the face of the detector. These events are random and occur rarely, which leads to the question of whether it is

possible to optimise this measurement setup to maximise the rate of these events and minimise the background fluctuations.

As figure 7.2 shows, the fluctuation amplitude increases with the source wire velocity above $v = v_c$. This suggests that to minimise the background fluctuations and observe a vortex line, we should measure at velocities near the critical velocity. However, after measuring in this way for a number of hours, we have not observed an event that indicates a single vortex line. Increasing the rate of events is more difficult to achieve, at least in this cell, as it isn't clear how a single vortex ring or line could be generated.

If we consider changes to the geometry of the cell to improve this measurement, the next logical step seems to be a setup with a vibrating wire perpendicular to the face of the detector. It has previously been shown [57] that turbulence propagates in the direction of motion of the wire, so this geometry would allow for turbulence to propagate past the face of the detector, and it could potentially be easier to detect vortex rings and lines. In addition, vortex rings can be reliably generated by vibrating grids [25], hence, a similar setup, but with a grid instead of a wire could be used to image vortex rings. In certain cases [4, 29], vibrating wires can generate vortex rings, but this appears dependent on either the profile of the wire, or it's surroundings.

Chapter 8

Summary

The work presented in this thesis focuses on the use of a novel two dimensional detector of quasiparticle excitations to investigate the properties of quasiparticle beams and quantum turbulence in superfluid ^{3}He-B. This is the first detector capable of measuring these in two spatial dimensions and with a much greater resolution then in previous measurements.

The detector was constructed from 5 arrays of 5 tuning forks mounted in a copper block to create a 25 pixel square detector of excitation flux. The forks were chosen such that their resonant frequencies span a range of 20 to 40kHz and each resonance has sufficient frequency spacing such that cross-talk between forks is minimised. The detector was situated in a cell such that it could be illuminated with a beam of thermal excitations, and that turbulence could be generated in the path of the beam, which will cast a shadow on the face.

We have investigated the angular profile of the quasiparticle beam generated by a black-body radiator. We show that the beam is well modelled by treating the BBR orifice as a point source of excitations, by fitting such a model along the central array of forks and to the central fork on each array. In addition, these fits show that the orifice of the box, designed to be directly in line with the central pixel, is actually offset by 0.48 mm in the horizontal direction and 0.1 mm in the vertical direction. This is due to the fact that the detector and accompanying vibrating wires were assembled by hand, on separate bases. We also observed that the angular spread of the BBR beam remains constant as the applied power is increased, consistent with the rapid thermalisation of quasiparticles inside the BBR cavity. This is also confirmation of a long-held assumption of the properties of the black-body radiator.

Measuring the width parameter of the tuning forks as a function of the power applied to the BBR radiator indicates that it is possible, in principle, to calibrate each pixel for bolometric measurements. This would be done by measuring the width parameter of the pixels as a function of the power entering them from the beam, and calibrating them in a similar manner to the BBR. This could then be used to directly measure the spatial variation of the power incident on the face of the detector.

We also measured the profile of the excitation beam generated by the source wire. In contrast to the beam emitted by the black-body radiator, the angular profile of this beam changes as the velocity of the wire increases, starting as a narrow beam

emitted from the apex of the wire loop, and widening as the velocity increases and the active area of the wire grows.

The source wire was also used to generate a turbulent tangle, which was illuminated by a beam from the BBR and cast a shadow on the face of the detector. We found that the shadow was greatest in the vicinity of the wire, and attributed this to the continuous emission of vortex rings from the wire. The shadow cast on the remainder of the detector was approximately uniform and indicated that the turbulence filled the entire volume illuminated by the beam. We observe this behaviour both near the critical velocity and at high wire velocities ($v \sim v_c$), the only difference being that the line density across the whole volume increases with velocity. In the vicinity of the wire, at $v = 2.5v_c$ we calculated the line density as $L = 3.4 \times 10^7$ m^{-2}, similar to that calculated for turbulence generated by a vibrating grid [52].

We investigated the development of the shadow as a function of the source wire velocity. These measurements show that the development of the shadow is reproducible across multiple experimental runs and independent of the power applied to the BBR beam, confirming that the beam is a passive probe. In addition there are reproducible features in the development of the shadow, but it is unclear where these originate from.

Measurements of fluctuations in the shadow cast by the vortex tangle show that the turbulence has a spectrum reminiscent of the Kolmogorov spectrum. We have

also shown that the resolution of the detector is such that it is capable of measuring the shadow cast by a single vortex line, and have examined possible candidates of such a measurement. These candidates show that with some refinement to the experimental techniques to further improve the noise, and further development of the detector and experimental setup would allow measurement of the fine structure of a vortex tangle and the propagation of vortex rings.

It is clear that a detector of quasiparticle flux is a device with great potential for the study of superfluid ^{3}He with further applications in the study of quantum turbulence, potential bolometric applications and for measuring properties of ^{3}He-A/^{3}He-B interfaces [59].

The detector, however, has limitations that could be improved in future iterations. The sensitivity of the tuning forks to thermal quasiparticles is lower than that of vibrating wires. A regular array of such vibrating wires would be much more difficult to build however. Micro-electromechanical [60, 61] and nano-electromechanical devices [62] are worth considering as a replacement, but have not been tested in ^{3}He-B sufficiently yet.

The pixel density could be increased in future iterations, this could allow measurement of finer structure within the turbulent tangle. However, this requires much smaller devices and would increase the complexity of the measurement setup. The size of the detector could be increased while maintaining the same pixel density. This could serve to allow better measurements of the time of flight of vortex rings and other structures.

In addition, the geometry of the devices surrounding the detector could be changed. For example two projections of the measurement of the spatial profile of turbulence could allow reconstruction of a three dimensional model of a tangle. This also requires two detectors, and for measurements such as this it would be convenient if the detector could be designed in such a way that would allow it to be made automatically, as the current design requires it to be hand-made and it would be difficult and time-consuming to build multiple detectors.

In addition to this, the BBR and detector could be mounted on movable platforms. This would allow the offset in the beam profiles to be corrected for. The orifice of the BBR could also be produced using a microfabricated membrane, which would allow much better control of the size of the orifice and the thickness of the wall, which would maximise the effective area of the hole.

Bibliography

[1] R.P. Feynman, R.B. Leighton, and M.L. Sands. *The Feynman Lectures on Physics*, volume I. Addison-Wesley, Reading, MA, 1963.

[2] D.I. Bradley, S.N. Fisher, A.M. Guénault, M.R. Lowe, G.R. Pickett, A. Rahm, and R.C.V. Whitehead. Quantum Turbulence in Superfluid ^{3}He Illuminated by a Beam of Quasiparticle Excitations. *Phys. Rev. Lett.*, 93:235302, December 2004.

[3] S.N. Fisher, A.J. Hale, A.M. Guénault, and G.R. Pickett. Generation and Detection of Quantum Turbulence in Superfluid ^{3}He-B. *Phys. Rev. Lett.*, 86(2):244–247, January 2001.

[4] D.I. Bradley, S.N. Fisher, A. Ganshin, A.M. Guénault, R.P. Haley, M.J. Jackson, G.R. Pickett, and V. Tsepelin. The Onset of Vortex Production by a Vibrating Wire in Superfluid ^{3}He-B. *J. Low Temp. Phys.*, 171(5-6):582–588, September 2012.

[5] D.I. Bradley, D.O. Clubb, S.N. Fisher, A.M. Guénault, R.P. Haley, C.J. Matthews, G.R. Pickett, V. Tsepelin, and K. Zaki. Decay of Pure Quantum Turbulence in Superfluid ^{3}He-B. *Phys. Rev. Lett.*, 96:035301, January 2006.

[6] D.I. Bradley, P. Crookston, S.N. Fisher, A. Ganshin, A.M. Guénault, R.P. Haley, M.J. Jackson, G.R. Pickett, R. Schanen, and V. Tsepelin. The Damping of a Quartz Tuning Fork in Superfluid ^{3}He-B at Low Temperatures. *J. Low Temp. Phys.*, 157:476–501, October 2009.

[7] V.M.H. Ruutu, U. Parts, J.H. Koivuniemi, N.B. Kopnin, and M. Krusius. Intrinsic and Extrinsic Mechanisms of Vortex Formation in Superfluid ^{3}He-B. *J. Low Temp. Phys*, 106(5-6):94–164, 1997.

[8] S.N. Fisher, M.J. Jackson, Y.A. Sergeev, and V. Tsepelin. Andreev reflection, a tool to investigate vortex dynamics and quantum turbulence in ^{3}He-B. *PNAS*, 111(Supplement 1):4659–4666, March 2014.

[9] S.N. Fisher, A.M. Guénault, C.J. Kennedy, and G.R. Pickett. Blackbody Source and Detector of Ballistic Quasiparticle in ^{3}He-B: Emission Angle from a Wire Moving at Supercritical Velocity. *Phys. Rev. Lett.*, 69(7):1073–1076, August 1992.

[10] D.I. Bradley, S. N. Fisher, A.M. Guénault, R.P. Haley, G.R. Pickett, D. Potts, and V. Tsepelin. Direct measurement of the energy dissipated by quantum turbulence. *Nature Phys.*, 7(6):473–476, April 2011.

[11] P.V.E. McClintock, D.J. Meredith, and J.K. Wigmore. *Matter at Low Temperatures*. Blackie Academic and Professional, 1984.

[12] A.M. Guénault. *Basic Superfluids*. Masters Series in Physics and Astronomy. Taylor and Francis, London and New York, 2003.

[13] D.S. Greywall. ^{3}He specific heat and thermometry at millikelvin temperatures. *Phys. Rev. B*, 33(11):7520–7538, June 1986.

[14] J. Bardeen, L.N. Cooper, and J.R. Schrieffer. Theory of Superconuctivity. *Phys. Rev.*, 108(5):1175–1204, December 1957.

[15] M. Tsubota. Quantum turbulence - from superfluid helium to atomic Bose-Einstein condensates. *J. Phys.: Condens. Matter*, 21:164207, March 2009.

[16] D. Page, M. Prakash, J.M. Latimer, and A.W. Steiner. Rapid Cooling of the Neutron Star in Cassiopeia A Triggered by Neutron Superfluidity in Dense Matter. *Phys. Rev. Lett.*, 106(8), February 2011.

[17] D.R. Tilley and J. Tilley. *Superfluidity and Superconductivity*. Van Nostrand Reinhold, 1974.

[18] R. Balian and N.R. Werthamer. Superconductivity with Pairs in a Relative p-Wave. *Phys. Rev.*, 131(4):1553–1564, August 1963.

[19] L. Landau. Theory of the Superfluidity of Helium II. *Phys. Rev.*, 60:356–358, August 1941.

[20] B. Lautrup. *Physics of Continuous Matter*. IoP Publishing, 2005.

[21] O. Reynolds. An Experimental Investigation of the Circumstances Which Determine Whether the Motion of Water Shall Be Direct or Sinuous, and of the Law of Resistance in Parallel Channels. *Phil. Trans. R. Soc. Lond.*, 174:935–982, 1883.

[22] O.V. Lounasmaa and E.V. Thuneberg. Vortices in rotating superfluid ^{3}He. *Proc. Natl. Acad. Sci. USA*, 96:7760–7767, July 1999.

[23] D. Vollhardt and P. Wolfe. *The Superfluid Phases of Helium 3.* Dover, 2013.

[24] Y. Kondo, J.S. Korhonen, M. Krusius, V.V. Dmitriev, E.V. Thuneberg, and G.E. Volovik. Combined Spin-Mass Vortex with Soliton Tail in Superfluid ^{3}He. *Phys. Rev. Lett.*, 68(22), June 1992.

[25] D.I. Bradley, D.O. Clubb, S.N. Fisher, A.M. Guénault, R.P. Haley, C.J. Matthews, G.R. Pickett, V. Tsepelin, and K. Zaki. Emission of Discrete Vortex Rings by a Vibrating Grid in Superfluid ^{3}He-B: a Precursor to Quantum Turbulence. *Phys. Rev. Lett.*, 95(3):035302–1–4, July 2005.

[26] R.J. Donelly. *Quantised Vortices in Helium II.* Cambridge University Press, 2005.

[27] R.E. Packard and J.C. Davis. Phase slip phenomena in superfluid helium. *Physica B*, 197:315–323, 1994.

[28] E. Varoqueaux and O. Avenel. Phase Slip Phenomena in superfluid helium. *Physica B*, 197:306–314, 1994.

[29] D.I. Bradley. Repetitive Single Vortex-Loop Creation by a Vibrating Wire in Superfluid ^{3}He-B. *Phys. Rev. Lett.*, 84(6):1252–1255, February 2000.

[30] A.N. Kolmogorov. The local structure of turbulence in incompressible viscous fluid for very large Reynolds numbers. *Proc. R. Soc. Lond. A*, 434:9–13, 1991.

[31] W.P. Halperin and M. Tsubota, editors. *Progress in Low Temperature Physics: Quantum Turbulence*. Elsevier BV, 2009.

[32] W.F. Vinen. How is turbulent energy dissipated in a superfluid. *J. Phys.: Condens. Matter*, 17:3231–3238, 2005.

[33] W.F. Vinen. Decay of superfluid turbulence at a very low temperature: The radiation of sound from a Kelvin wave on a quantized vortex. *Phys. Rev. B*, 64(13):134520, Sep 2001.

[34] A.W. Baggaley, C.F. Barenghi, and Y.A. Sergeev. Quasiclassical and ultra-quantum decay of superfluid turbulence. *Phys. Rev. B*, 85(6):060501, Feb 2012.

[35] G.R. Pickett. Microkelvin Physics. *Rep. Prog. Phys.*, 51:1295–1340, March 1988.

[36] D.J. Cousins, S.N. Fisher, A.M. Guénault, R.P. Haley, G.R. Pickett, G.N. Plenderleith, P. Skyba, P.Y.A. Thibault, and M.G. Ward. An Advanced Dilution Refrigerator Designed for the New Lancaster Microkelvin Facility. *J. Low Temp Phys*, 114(5-6):547–570, 1999.

[37] E.A. Guise. *Developing a Quasiparticle Detector for Quantum Turbulence Imaging Studies in Superfluid ^{3}He-B*. PhD thesis, Lancaster University, 2014.

[38] J. Jager, B. Schuderer, and W. Schoepe. Turbulent and Laminar Drag of Superfluid Helium on an Oscillating Microsphere. *Phys. Rev. Lett.*, 74(4):566–569, January 1995.

[39] M. Človečko, E. Gažo, M. Kupka, M. Skyba, and P. Skyba. High Quality Tuning Forks in Superfluid ^{3}He-B Below 200 μK. *J. Low Temp. Phys.*, 162:669–677, 2011.

[40] D.I. Bradley, M. Človečko, S.N. Fisher, D. Garg, E. Guise, R.P. Haley, O. Kolosov, G.R. Pickett, and V. Tsepelin. Crossover from hydrodynamic to acoustic drag on quartz tuning forks in normal and superfluid ^{4}He. *Phys. Rev. B*, 85:014501, January 2012.

[41] K. Karrai and R.D. Grober. Tip-sample distance control for near-field scanning optical microscopes. *SPIE*, 2535:69–81, 1995.

[42] M. Blažková, D. Schmoranzer, and L. Skrbek. Transition from laminar to turbulent drag in flow due to a vibrating quartz fork. *Phys Rev. E*, 75:025302, February 2007.

[43] M. Blažková, M. Človečko, E. Gažo, L. Skrbek, and P. Skyba. Quantum Turbulence Generated and Detected by a Vibrating Quartz Fork. *J. Low Temp. Phys.*, 148:305–310, May 2007.

[44] D.I. Bradley, M. Človečko, E. Gažo, and P. Skyba. Probing Andreev Reflection in Superfluid ^{3}He-B Using a Quartz Tuning Fork. *J. Low Temp. Phys.*, 152:147–155, July 2008.

[45] J.H. Staudte. Subminiature Quartz Tuning Fork Resonator. *Statek Corporation*, 1973.

[46] S. Holt and P. Skyba. Electrometric direct current I/V converter with wide bandwidth. *Rev. Sci. Instrum.*, 83:064703, 2012.

[47] R. Blaauwgeers, M. Blazkova, M. Človečko, V.B. Eltsov, R. de Graaf, J. Hosio, M. Krusius, D. Schmoranzer, W. Schoepe, L. Skrbek, P.Skyba, R.E. Solntsev, and D.E. Zmeev. Quartz Tuning Fork: Thermometer, Pressure- and Viscometer for Helium Liquids. *J. Low Temp. Phys.*, 146(5-6):537–562, February 2007.

[48] D.I. Bradley, P. Crookston, M.J. Fear, S.N. Fisher, G. Foulds, D. Garg, A.M. Guénault, E. Guise, R.P. Haley, O. Kolosov, G.R. Pickett, R. Schanen, and V. Tsepelin. Measuring the Prong Velocity of Quartz Tuning Forks Used to Probe Quantum Fluids. *J. Low Temp. Phys.*, 161:536–547, October 2010.

[49] Shih S. Chuang. Quartz Tuning Fork Crystal Using Overtone Flexure Modes. *Proc. 35th Ann. Freq. Control Symposium*, pages 130–143, May 1981.

[50] S.L. Ahlstrom, D.I. Bradley, M. Človečko, S.N. Fisher, A.M. Guénault, E.A. Guise, R.P. Haley, O. Kolosov, P.V.E. McClintock, G.R. Pickett, M. Poole,

V. Tsepelin, and A.J. Woods. Frequency-dependent drag from quantum turbulence produced by quartz tuning forks in superfluid ^{4}He. *Phys. Rev. B*, 89(1):014515, Jan 2014.

[51] S. N. Fisher. *The Mechanical Properties of Superfluids ^{3}He-A and ^{3}He-B in the Ballistic Regime*. PhD thesis, Lancaster University, 1991.

[52] M.J. Jackson. *A Study of Quantum Turbulence in Superfluid ^{3}He-B Using Vibrating Structures*. PhD thesis, Lancaster University, 2011.

[53] C.J. Lambert. Theory of pair breaking by vibrating macroscopic objects in superfluid ^{3}He. *Physica B*, 178:294–303, 1992.

[54] A. Calogeracos and G.E. Volovik. Critical velocity in ^{3}He-B vibrating wire experiments as analog of vacuum instability in a slowly oscillating electric field. *J. Exp. Theor. Phys.*, 88(1):40–45, January 1999.

[55] C.A.M. Castelijns, K.F. Coates, A.M. Guénault, S.G. Mussett, and G.R. Pickett. Landau Critical Velocity for a Macroscopic Object Moving in Superfluid ^{3}He-B: Evidence for Gap Suppresion at a Moving Surface. *Physical Review Letters*, 56:69–72, 1986.

[56] C. Bäurle, Yu.M. Bunkov, and S.N. FS.N. Fisher. Godfrin. Temperature scale and heat capacity of superfluid ^{3}He-B in the 100 μK range. *Phys Rev B*, 57(22):14382–14386, June 1998.

[57] D.I. Bradley, S.N.Fisher, A.M. Guénault, M.R. Lowe, G.R. Pickett, and A. Rahm. Spatial extent of quantum turbulence in non-rotating superfluid ^{3}He-B. *Physica B*, 329-333:104–105, 2003.

[58] Shoji Fujiyama and Makoto Tsubota. Vortex Line Density Fluctuations of Quantum Turbulence. *J. Low Temp Phys*, 158(3-4):428–434, Jul 2009.

[59] D.J. Cousins, M.P. Enrico, S.N. Fisher, S.L. Phillipson, G.R. Pickett, N.S. Shaw, and P.J.Y. Thibault. Probing the A-B Phase Interface in Superfluid ^{3}He by Andreev Reflection of a Quasiparticle Beam. *Phys. Rev. Lett.*, 77(26):5245–5248, December 1996.

[60] M. Gonzalez, P. Zheng, B.H. Moon, E. Garcell, Y. Lee, and H.B. Chan. Unusual Behavior of a MEMS Resonator in Superfluid ^{4}He. *J. Low Temp Phys*, 171(3-4):200–206, August 2013.

[61] E. Collin, L. Filleau, T. Fournier, Yu.M. Bunkov, and H. Godfrin. Silicon Vibrating Wires at Low Temperatures. *J. Low Temp. Phys.*, 150:739–790, January 2008.

[62] E. Collin, J. Kofler, J.-S. Heron, O. Bourgeois, Yu. M. Bunkov, and H. Godfrin. Novel Vibrating Wire Like NEMS and MEMS Structures for Low Temperature Physics. *J. Low Temp Phys*, 158(3-4):678–684, Sep 2009.